

Studies of stabilization technique for field-reversed configuration  
by using magnetized plasmoid injection  
(磁化プラズモイド入射による磁場反転配位プラズマの安定化手法に関する研究)

by  
Hiroto~~mo~~ Itagaki  
板垣 宏知

A Doctoral Dissertation  
博士論文

Submitted to  
the Department of Complexity Science and Engineering  
The University of Tokyo  
on December 2013

**Thesis Supervisor : Michiaki Inomoto 井通暁**  
**Title : Associate Professor of Complexity Science and Engineering**

## Abstract

Field-reversed configuration (FRC) is one of the so-called “compact torus” plasmas. The FRC has attractive features as high beta, unnecessary of central structure penetrating the plasma, natural diverter and linear device geometry. A rotational instability with toroidal mode number  $n = 2$  mode has been known as the most destructive instability for a FRC generated by a FRTP method, and the lifetime of FRC has been severely restricted by this instability.

Some suppression methods for the elliptic deformation have been investigated by experimental and numerical studies, however, no decisive scheme has been developed. In fact, the spontaneous spin-up mechanism itself has not been fully understood. In this paper, I proposed a new control method for the rotational instability by using double-sided magnetized plasmoid injection technique. By changing the polarity of the two plasmoid's toroidal fields, two operation modes are available; poloidal flux injection and poloidal flux and toroidal flux injection.

Suppression of the elliptic deformation was observed not only in the poloidal flux and toroidal flux injection case but also in the poloidal flux injection case. This result indicates that the poloidal flux injection provides the dominant impact in the stabilization. To clarify the stabilization mechanism, toroidal flow velocity measurements have been carried out. The plasmoid injection certainly reduced the spontaneous spin-up of the FRC, resulting in mitigation of the elliptic deformation. The variation of the angular velocity showed good correlation with the variation of the trapped flux, suggesting that the spontaneous spin-up could be induced by the flux decay of the FRC plasma.

In conclusion, a new control method for rotational instability of the FRC plasma has been developed. The proposed method is capable of reducing the rotation velocity of a FRC, mitigating the elliptic deformation and eventually extending the FRC discharge duration.

## Contents

<b>1. Introduction</b>	<b>P1-P4</b>
1.1. Back ground.....	P1
1.2. Suppression of rotational instability.....	P2
1.3. Target of this work.....	P3
1.4. Outline of this thesis.....	P3
<b>2. Rotational instability in FRC</b>	<b>P5-P19</b>
2.1. Overview of the rotational instability.....	P5
2.2. Possible spin-up mechanisms.....	P6
2.2.1. Selective particle loss.....	P6
2.2.2. End shorting.....	P12
2.2.3. Poloidal flux decay.....	P18
<b>3. Experimental setup</b>	<b>P20-P45</b>
3.1. Overview of NUCTE-III device.....	P20
3.2. Formation scheme of FRC.....	P22
3.3. Plasma parameters of FRC.....	P24
3.3.1. Separatrix radius and separatrix length.....	P24
3.3.2. Plasma volume.....	P26
3.3.3. Magnetic axis.....	P26
3.3.4. Plasma beta.....	P28
3.3.5. Poloidal flux.....	P30
3.3.6. Total temperature.....	P31
3.3.7. The value of $s$ .....	P32
3.4. Measurement system.....	P33
3.4.1. Magnetic field and flux diagnostic.....	P33
3.4.2. Emission measurement by photo-multiplier tube system.....	P36

3.4.3.	He-Ne laser interferometer.....	P38
3.4.4.	Doppler spectroscopy.....	P42
4.	Development and Performance of MCPG	P46-P58
4.1.	Formation schema of magnetized plasmoid.....	P46
4.2.	Characteristic of MCPG mounted on the NUCTE.....	P47
4.3.	Discharge motions for MCPG.....	P49
4.4.	Magnetic helicity produced by MCPG.....	P50
4.5.	Performance test of a plasma gun.....	P52
4.5.1.	Typical discharge waveform.....	P52
4.5.2.	Traveling speed of the plasmoid.....	P52
4.5.3.	Magnetic field measurement of the plasmoid.....	P55
5.	Results from Single plasmoid Injection Experiment	P59-P62
5.1.	Single plasmoid injection for FRC.....	P59
5.2.	Experimental results of single side injection.....	P59
5.3.	Discussion for single side injection.....	P61
6.	Results from Double side Injection Experiment	P63-72
6.1.	Conditions for plasmoid injection into FRC.....	P63
6.2.	Typical discharge sequence with NUCTE-III and MCPG .....	P64
6.3.	Impact of neutral gas from MCPG.....	P66
6.4.	Experimental results of double side injection.....	P67
6.4.1.	Difference of time evolutions of separatrix radius and poloidal flux.....	P67
6.4.2.	Stablization effect on rotational instability.....	P70
7.	Discussion	P73-P87
7.1.	Evaluation of plasmoid's energy and inventory.....	P73
7.2.	Comparison between Single injection and Double injection....	P75
7.3.	Poloidal flux increment dependence on gun voltage and bias field.....	P78

7.4. Suppression effect on FRC's toroidal rotation.....	P80
7.5. Flux decay theory and stabilization effect by plasmoid injection.....	P84
7.6. Summary of the discussion.....	P87
8. Conclusion	P88-P103
8.1. Summary of the chapters of this thesis.....	P88
8.2. Conclusion of this experimental research.....	P90
Acknowledgement.....	P92-P93
Research achievement.....	P94-P97

# 1. Introduction

## 1.1. Background

A FRC (Field-Reversed Configuration) [1,2] is one of the so-called “compact torus” plasmas which do not require central structures penetrating the plasma. It has extremely highly beta value ( $\beta \sim 1$ ) compared with tokamak or helical type confinements. The beta is defined as a ratio of the plasma thermal pressure to the magnetic pressure and indicates coefficient of magnetic field utilization to sustain plasma pressure. Since the plasma pressure is sustained solely by poloidal magnetic field, the FRC’s equilibrium is obtained only in high beta regime close to unity. Fusion power plant concepts [3] using advanced fuels such as D-D or D-<sup>3</sup>He have been proposed as an application of FRC plasma for fusion core because the FRC’s high beta will reduce the synchrotron radiation loss in high temperature region which is required for advanced fuel fusion reaction.

FRTP (Field Reversed Theta Pinch) technique [4] has been utilized to produce high temperature ( $\sim 1$  keV) and high particle density ( $\sim 10^{22}$  m<sup>-3</sup>) FRC plasma. Typical theta-pinch based FRC device consists of a quartz discharge tube and theta pinch coil surrounding the discharge tube, as illustrated in fig.1.1. The FRC structure has open and closed field regions. These regions are separated by the separatrix surface. High temperature plasma is dominantly confined inside the separatrix. Axial magnetic field reverses at the magnetic axis, thus the axis is also called as a null (O) point. In fig.1.1, major radius  $R$  expresses the radius of the magnetic axis from device center, the separatrix radius  $r_s$  indicates the radius of separatrix on the mid plane. The poloidal field

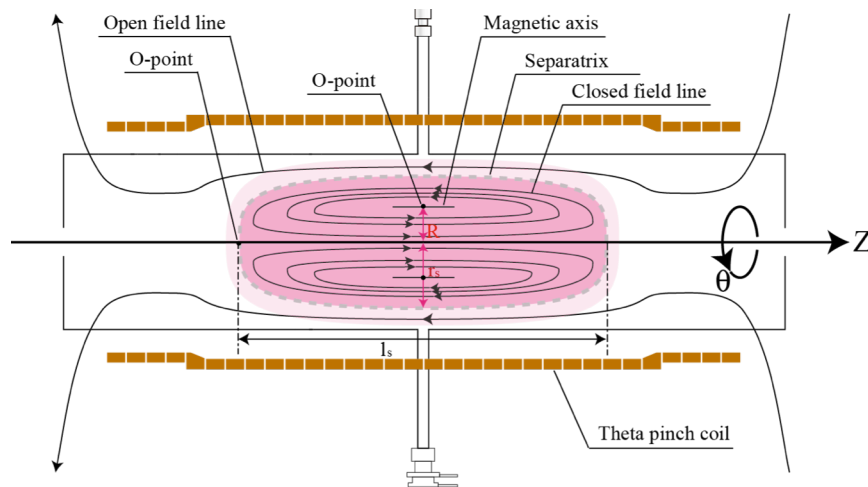


Fig.1.1 Schematic view of FRC and theta pinch device

is formed by toroidal plasma current and no poloidal plasma current or toroidal field exists. Though the FRC formed by FRTP method has quite high pressure (or high beta value), its life time is restricted to be less than 0.5ms by a destructive instability called “rotational instability” [5] associated with toroidal mode number of  $n=2$  deformation of the plasma cross section. The origin of this global instability is the spontaneous rotation of the FRC plasma. The FRC plasma almost always starts to rotate in ion’s diamagnetic direction just after it reaches equilibrium and spins up until it starts elliptical deformation due to the centrifugal force. The deformation grows nonlinearly and finally the plasma hits the wall and collapses. Thus development of an effective suppression method for the rotational instability is the most urgent issue in the FRC fusion research.

## 1.2. Suppression of rotational instability

Although the physical mechanism of the spontaneous rotation has not clarified yet, three major schemes have been recognized as suppression methods of the destructive rotational instability. The one is the application of a multi-pole magnetic field [6]. In this method, a multi-pole field is applied externally on the FRC plasma. The azimuthally non-uniform multi-pole field acts on the surface of the FRC plasma to recover the elliptical deformation by the centrifugal force. However, this multi-pole field usually causes a negative effect on FRC confinement and should not be used in the recent high-performance FRC discharge [7].

Recently, active control of radial electric field was performed to stabilize the rotational instability [10]. Coaxial electrodes mounted on both ends of the FRC were utilized to apply voltage between open magnetic field lines outside of the FRC’s separatrix. The  $E \times B$  counter rotation driven by the applied radial electric field was supposed to stabilize the FRC’s self-rotation.

The other stabilization mechanism is provided by a modest toroidal magnetic field induced in the FRC plasma. This stabilizing effect was first demonstrated in an axial translation experiment [8] and then numerically confirmed by MHD simulation study [9]. During the acceleration phase of FRC, a net toroidal field is induced (in other words, the toroidal field do not perfectly cancel out in the translation case) inside the FRC. This toroidal field is so small that it does not change the high beta property of FRC.

### 1.3. Target of this work

In this study, a novel active control method for stabilizing the rotational instability has been proposed and the mechanism which accelerates the plasma rotation has been investigated. As for the existing stabilization methods, the former two methods using multi-pole field and radial biasing are symptomatic ways to decelerate the plasma rotation. They have not provided any valuable knowledge on the spontaneous generation of FRC rotation. The multi-pole field also has disadvantage on confinement. The third mechanism of the modest toroidal field works to improve the stability against the rotational mode; however, the generation of the toroidal field by axial translation is a transient technique and cannot be sustained for a long time.

For the purpose of future long-lived FRC experiment, novel control method for stabilizing the plasma rotation is strongly required. In this study, magnetized plasmoid injection was employed as a potential candidate to control the FRC rotation. MCPGs (Magnetized Coaxial Plasma Guns) were developed to supply magnetized plasmoid with necessary parameters for stabilization.

### 1.4. Outline of this thesis

In Chapter 2, earlier studies on the FRC spontaneous rotation and the rotational instability will be reviewed. Theoretical interpretation and several candidates for an origin of the rotation will be described.

In Chapter 3, setup of the FRC experiment will be described. In this study, NUCTE-III device in Nihon University was employed to form high beta FRC by the FRTP method. Descriptions of FRC equilibrium based on classical model and basic diagnostic used in this study will also be given.

In Chapter 4, development of MCPG performed in this study will be described. Detailed design of the developed MCPG, performance test of the MCPG and evaluation of achieved plasmoid will be presented.

In Chapter 5, experimental result of single side plasmoid injection will be described. Reaction of FRC on injection will be evaluated.

In Chapter 6, results from double side injection will be described. The plasma response on two different injection cases will be investigated.

In Chapter 7, possible stabilization mechanism will be discussed based on the results presented in Chapters 5 and 6.

Finally conclusion of this study will be given in Chapter 8.

- [1] M. Tuszewski, Nucl. Fusion **28**, 2033 (1988)
- [2] L.C. Steinhauer, Phys. Plasma **18**, 070501 (2011)
- [3] H. Momota , et al., Fusion Tech. **21**, 2307 (1992).
- [4] A.L. Hoffman, R.D. Milroy, J.T. Slough, L.C. Steinhauer, Fusion Technol. **9**, 48 (1986)
- [5] F.C. Jahoda, E.M. Little, W.E. Quinn, F.L. Ribe, G.A. Sawyer, J. Appl. Phys. **35**, 2351(1964)
- [6] D.J. Rej, et al, Phys. Fluids **29**, 8 (1986)
- [7] H.Y Guo, et al., Phys. Plasma **18**, 056110 (2011).
- [8] H.Y. Guo, et al., PRL **95**, 175001 (2005).
- [9] R.D.Milroy, L.C.Steinhauer, Phys.plasma. **15**,022508 (2008)
- [10] M. Tuszewski, et al., PRL **108**, 255008 (2012).

## 2. Rotational instability in a FRC

### 2.1. Overview of the rotational instability

The MHD (Magnetohydro Dynamics) theory has predicted that a FRC is unstable for instabilities of low  $n$  toroidal mode. The FRC has various theoretically predicted instabilities such as external and internal tilt instabilities and rotational instability. Although the internal tilt instability of toroidal mode number  $n = 1$  mode has been predicted unstable, the tilt instability has never been observed experimentally [1-3]. As the mechanism of stabilization, FLR (Finite Lamor Radius) effect and non-linear saturation effect have been proposed [4]. On the other hand, the FRC spontaneously rotates in toroidal direction. Since a centrifugal force is exerted on rotated FRC, deformation of toroidal cross section is grown if the cross section is deformed from a circle. The rotational instability, which is one of inter-change instabilities with toroidal mode number of  $n = 2$ , is caused by a centrifugal force of rapidly rotating plasma, and the instability has been known as the most destructive instability of a FRC [5]. The centrifugal force causes an explosive growth of the elliptic deformation. Eventually the FRC configuration is also disrupted.

The growth of rotational instability has a threshold value of  $\alpha$ . The  $\alpha$  is expressed as

$$\alpha \equiv \frac{\Omega}{\Omega_{Di}} \quad (1)$$

, where  $\Omega$  is the rotation frequency of FRC and  $\Omega_{Di}$  is the ion diamagnetic drift frequency [5]. The  $n = 2$  mode grows when the  $\alpha$  is greater than 1.2 – 1.4 [5]. In addition, W. Saylor predicted that the  $n = 2$  mode grows faster when the  $\alpha$  is greater than 1.3 – 1.5 [6]. Also FRX-B device has demonstrated that the  $n = 2$  mode grew when the  $\alpha$  greater than 1.6 [7].

The origin of the rotation has been researched by theoretically and experimentally, and several possible mechanisms have approached to explain the spin-up of FRC. In this chapter, the possible spin-up mechanisms are introduced. The stabilization experiments of rotational instability are also introduced.

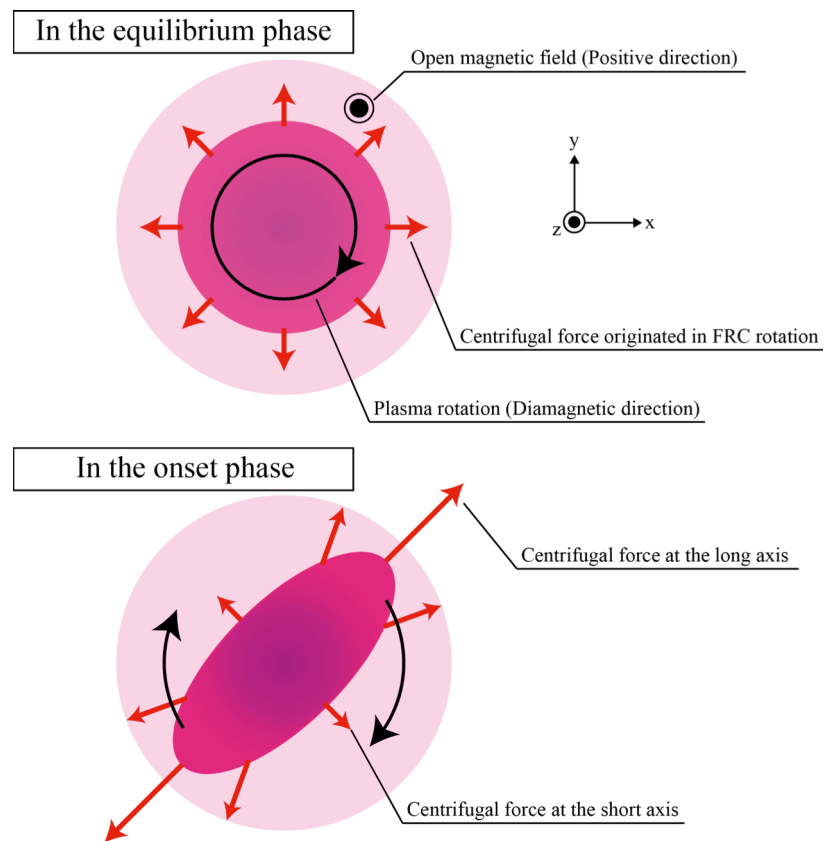


Fig.2.1. Schematic view of an elliptic deformation.

## 2.2. Possible spin-up mechanisms

### 2.2.1. Selective particle loss

This theory has been suggested by Barnes and Seyler [8]. Charged particles, which move in FRC, feel a magnetic field and achieve a drift velocity such as diamagnetic drift, curvature drift, grad-B drift and electric drift. Since a poloidal field

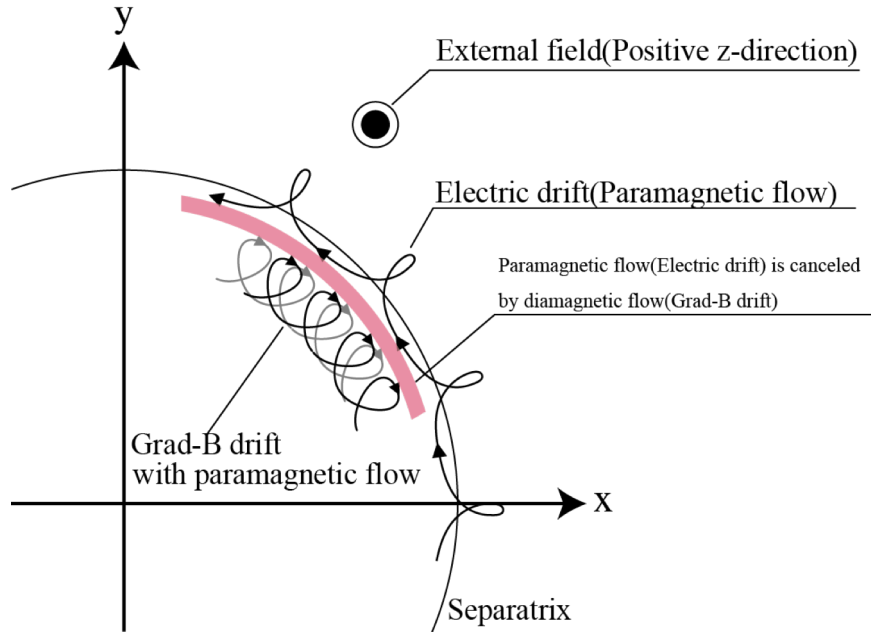


Fig.2.2. Cancellation mechanism of paramagnetic flow by diamagnetic component of grad-B drift

line is approximated straight magnetic field line in toroidal cross section of the mid-plane area, curvature drift was ignored in this consideration.

In this consideration, poloidal flux  $\Psi$  was defined to be greater than zero outside the separatrix. In addition, it was supposed that ion has a non-rotating Maxwell distribution at each location initially and electron was regarded as no inertia fluid. Consequently, the density profile is required to be a configuration in which ion electric drift is cancelled by an ion diamagnetic flow.

Near the separatrix, the direction of electric drift is the paramagnetic direction as shown in fig.2.2. The electric drift of an ion whose guiding center exists outside the separatrix also has a paramagnetic direction. This paramagnetic flow is canceled by diamagnetic drift or grad-B drift that has diamagnetic direction in some case. In the equilibrium phase, the paramagnetic flow of electric drift and diamagnetic flow is

balanced. However if the ions whose guiding center located on open field line escaped along open magnetic field line, angular momentum of paramagnetic direction is also lost. Therefore diamagnetic flow and paramagnetic flow are not balanced, and the FRC starts to rotate with diamagnetic direction. This rotation is caused inside the separatrix radius and the width of effective region is equal to the gyro radius.

This picture was described by Hamed and Hewett theoretically [9]. In this calculation, the loss of an ensemble of particles whose guiding center is outside of the separatrix radius has been evaluated assuming that center of mass of the particles is at their guiding center. Under the conditions, loss of angular momentum is expressed as

$$L_{lost} = \sum_{i=1}^N r_i \times m_i v_i \quad (2)$$

, where  $r_i$  is the particle radius,  $m_i$  is the particle mass and  $v_i$  is the particle velocity. Furthermore,  $r_i$  and  $v_i$  are also expressed as follows

$$r_i = r_s + r_i' , \quad (3)$$

$$v_i = v_d + v_i' \quad (4)$$

, where  $r_s$  is separatrix radius,  $r_i'$  is gyro radius,  $v_d$  is drift velocity and  $v_i'$  is gyro velocity. Therefore lost angular momentum is expressed substituting the eq.(2-3) and eq.(2-4) into eq.(2-2) as

$$L_{lost} = \sum_{i=0}^N (r_s + r_i') \times m_i (v_d + v_i') \quad (5)$$

$$\begin{aligned} L_{lost} &= \sum r_s \times m_i v_d + \sum r_i' \times m_i v_i' \quad (6) \\ &+ \left( \sum m_i r_i' \right) \times v_d \\ &+ r_s \times \left( \sum m_i v_i' \right). \end{aligned}$$

Since  $r_s$  is a center of mass, last two terms of eq.(2-6) vanish. Then eq.(2-6) becomes

$$L_{lost} = Nm_i \left( r_s v_{0d} - \frac{2v_t \rho_i}{\sqrt{1 - \beta}} \right) \quad (7)$$

, where  $v_{0d}$  is drift velocity,  $v_t$  thermal velocity and  $\rho_i$  is ion gyro radius. Since the gyro radius  $\rho_i$  is evaluated using the magnetic field at chamber wall, the factor of  $\sqrt{1 - \beta}$  appears in eq.(2-7). Here,  $v_{0d}$  is defined as a sum of grad-B drift and electric drift. To consider the eq.(2-7), diamagnetic drift and  $v_{0d}$  are required to calculate. The diamagnetic drift frequency is expressed as

$$\begin{aligned} \Omega_* &= \frac{1}{neBr_s} \frac{dp}{dr} \quad (8) \\ &= \frac{1}{2\mu_0} \frac{B}{er_s n} \frac{d\beta}{dr} \end{aligned}$$

$$\Omega_* = \frac{v_t \rho_i}{r_s \beta \sqrt{1 - \beta}} \frac{\partial \beta}{\partial r} \quad (9)$$

assuming the radial pressure balance of FRC. In addition, electric drift frequency of  $\Omega_{DE}$  is described by rotating frequency of  $\Omega$  and the diamagnetic frequency of  $\Omega_*$  as

$$\Omega_{DE} = \Omega - \Omega_* \quad (10)$$

$$\Omega_{DE} = (\alpha - 1)\Omega_*$$

, where  $\alpha$  is defined as eq.(2-1). Therefore electric velocity of  $v_E$  at separatrix radius is expressed as

$$v_E = r_s (\alpha - 1) \Omega_* \quad (11)$$

Grad-B drift is also expressed as

$$\begin{aligned} v_{\nabla B} &= \frac{1}{2} m_i v_t^2 \frac{1}{e B^2} \frac{\partial B}{\partial r} \\ &= r_s \beta \Omega_* \frac{1}{B} \frac{\partial B}{\partial r} \bigg/ \frac{\partial \beta}{\partial r} \\ &= \frac{r_s \beta}{B} \Omega_* \frac{\partial B}{\partial r} \frac{B}{2(1 - \beta)} \bigg/ \frac{\partial B}{\partial r} \end{aligned} \quad (12)$$

$$v_{\nabla B} = \frac{r_s \beta}{2(1 - \beta)} \Omega_*. \quad (13)$$

Here, we have achieved two expressions for the velocity of electric drift and grad-B drift expressed by diamagnetic frequency of  $\Omega_*$ . Substituting eq.(2-11) and eq.(2-13) into  $v_{0d}$ , drift velocity is achieved as

$$v_{0d} = v_E + v_{\nabla B} \quad (14)$$

$$v_{0d} = -\frac{v_t \rho_i}{\beta \sqrt{1 - \beta}} \left\{ 1 - \alpha + \frac{\beta}{2(1 - \beta)} \right\} \frac{\partial \beta}{\partial r}.$$

Substituting the eq.(2-14) into eq.(2-7), lost angular momentum is described as

$$L_{lost} = \frac{Nm_i v_t \rho_i}{\sqrt{1 - \beta}} \left[ \frac{r_s}{\beta} \frac{\partial \beta}{\partial r} \left\{ 1 - \alpha + \frac{\beta}{2(1 - \beta)} \right\} + 2 \right]. \quad (15)$$

Consequently, FRC loses the positive angular momentum estimated by eq.(2-15) when the N particles are lost at separatrix radius. In this theory, positive angular momentum loss is not produced if the rotation frequency of FRC is sufficiently fast.

### 2.2.2. End shorting

This theory has been proposed by L.C. Steinhauer [10-12]. In this section, the end shorting theory is introduced. FRC has closed field lines (confinement region) and open field lines. The open field lines are extended to end region of theta pinch device, and the field line possibly touches to metallic end flange as shown in fig.2.3 (b). This shorting is caused at a certain moment, and in a very short time. When the open field line intersects the metallic boundary, electric potential of separatrix surface is changed to generate radial electric field in FRC. This radial electric field has an outward direction and it generates an electric drift with diamagnetic direction.

In steady state FRC, the drift velocity perpendicular to magnetic field is expressed as the sum of diamagnetic drift and electric drift as

$$\begin{aligned} \mathbf{v}_{\perp a} &= \frac{\mathbf{E} \times \mathbf{B}}{B^2} + \frac{1}{nq_a} \frac{\mathbf{B} \times \nabla p_a}{B^2} \\ &= \frac{1}{B^2} \left( \mathbf{B} \times \nabla \phi + \frac{1}{nq_a} \mathbf{B} \times \nabla p_a \right) \end{aligned} \quad (16)$$

, where  $\mathbf{E}$  is an electric field,  $\mathbf{B}$  is a magnetic field,  $n$  is particle density,  $q_a$  is electric charge,  $p_a$  is a thermal pressure and  $\phi$  of fluid species  $a$  is an electric potential. Adopting a straight magnetic field line approximation for the mid-plane of FRC, then eq.(2-16) becomes

$$v_{Da} = \frac{1}{B} \frac{d\phi}{dr} + \frac{1}{q_a n B} \frac{dp_a}{dr} . \quad (17)$$

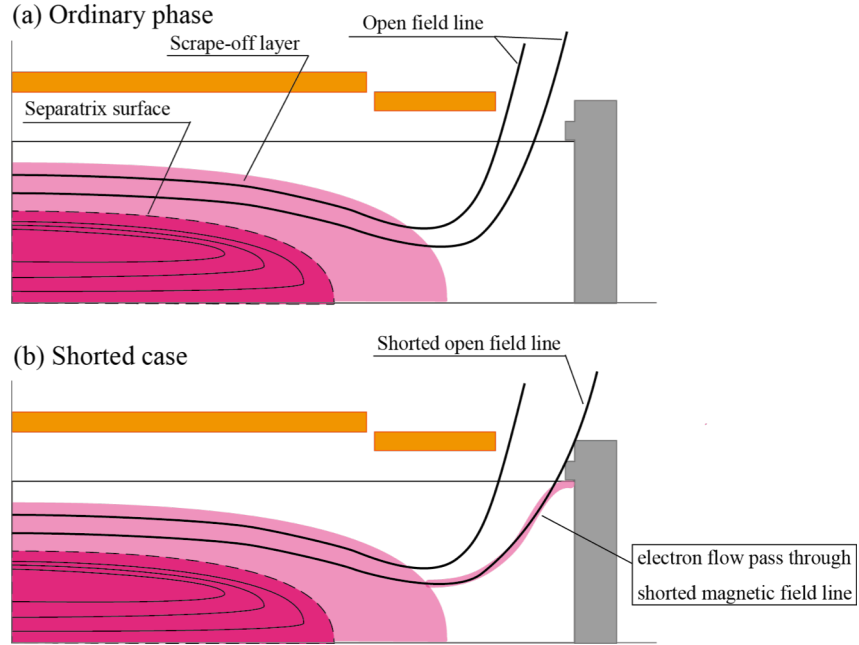


Fig.2.3. Schematic view of end shorting by open magnetic field line

Here, the relative gradients of the temperature and density is introduced, which is defined as

$$\eta_a \equiv \frac{d(\ln T_a)}{d(\ln n)} . \quad (18)$$

Some other parameters are introduced as follows: the local density length scale of

$$L_n = \left[ \left( -\frac{1}{n} \right) \frac{dn}{dr} \right]^{-1} , \quad (19)$$

the ion skin depth of

$$l_i \equiv \sqrt{\frac{m_i}{\mu_0 e^2 n}}, \quad (20)$$

The species beta of

$$\beta_a = \frac{2\mu_0 n k T_a}{B^2} \quad (21)$$

and the Alfvén velocity of

$$V_A = \frac{B}{\sqrt{\mu_0 n m_i}}. \quad (22)$$

By using formulate from the eq.(2-18) to eq.(2-22), diamagnetic drift velocity of  $V_{DM}$  is described as

$$V_{DM} = \frac{1}{q_a n B} \frac{dp_a}{dr} \quad (23)$$

$$= \frac{1}{q_a B} \left( \frac{dkT_a}{dr} + \frac{kT_a}{n} \frac{dn}{dr} \right)$$

$$= -\frac{1}{L_n} \frac{kT_a}{q_a B} (1 + \eta_a)$$

$$= -\frac{\beta_a}{2L_n} \frac{B}{\mu_0 n q_a} (1 + \eta_a)$$

$$V_{DM} = -(1 + \eta_a) \beta_a \frac{V_A}{2} \frac{l_i}{L_n}. \quad (24)$$

On the other hand, electric potential is estimated from eq.(2-17). If the pressure gradients and the rotation speed are achieved, the electric potential can be estimated.

In this process, end shorting causes a change in radial electric field. This modified electric field is achieved by solving the parallel electron equation of motion, which is expressed as

$$0 = -\nabla_{\parallel} p_e + en \nabla_{\parallel} \phi \quad (25)$$

assuming that electron mass and Lorentz-force are negligible and the electron is in steady state. Additionally, electron temperature is assumed to have a flat distribution along the magnetic field line when the electrons are not highly collisional. Thus eq.(2-25) becomes

$$0 = -kT_e \nabla_{\parallel} n_e + en \nabla_{\parallel} \phi \quad (26)$$

$$0 = -\frac{kT_e}{n_e} \nabla_{\parallel} n_e + e \nabla_{\parallel} \phi$$

$$\nabla_{\parallel} \left[ -\left(\frac{kT_e}{e}\right) \ln n_e + \phi \right] = 0. \quad (27)$$

To integrate eq.(2-27), the equation for electric potential is achieved as

$$\phi = \left(\frac{kT_e}{e}\right) \ln n_e + \phi_0(\psi) \quad (28)$$

, where the  $\phi_0$  is a integration constants which depends on poloidal flux surface and indicates a potential at the end boundary. Therefore  $\phi_0$  is constant value while the end shorting process. Thus the radial electric field is achieved by differentiating the eq.(2-28). Then the electric field is calculated as

$$E_r = -\frac{d\phi}{dr} \quad (29)$$

$$\begin{aligned} &= -\frac{k}{e} \left( \ln n_e \frac{dT_e}{dr} + \frac{T_e}{n_e} \frac{dn_e}{dr} \right) \\ &= \frac{kT_e}{eL_n} \left[ \frac{d(\ln T_e)}{d(\ln n_e)} + 1 \right] \\ E_r &= \frac{kT_e}{e} (1 + \eta_e) \frac{1}{L_n} . \end{aligned} \quad (30)$$

Furthermore, relative gradients and local density length scale satisfy the following conditions near the separatrix: relative gradients  $\eta_e > 0$  and local density length scale  $L_n > 0$ . Since radial electric field of  $E_r$  has positive sign by using above condition of  $\eta_e$  of and  $L_n$ , end shorting causes a reversal of sign of the radial electric field. Hence, end shorting changes the direction of electric drift from paramagnetic to diamagnetic. The electric drift speed is calculated by using the first term of eq.(2-17) and eq.(2-30) as follows

$$\begin{aligned} v_E &= \frac{1}{B} \frac{d\phi}{dr} \\ &= -\frac{1}{B} \frac{kT_e}{e} (1 + \eta_e) \frac{1}{L_n} \end{aligned} \quad (31)$$

$$v_E = -(1 + \eta_e) \beta_e \frac{V_A}{2} \frac{l_i}{L_n} . \quad (32)$$

Consequently drift motion in diamagnetic direction is expressed as the sum of electric drift and diamagnetic drift when end shorting is occurred as shown in fig.2.4. Spin-up

of end shorting is supposed to have two processes: first, the reversed radial electric field drives diamagnetic flow near the separatrix, and then the ion flow inside the separatrix is driven through a friction.

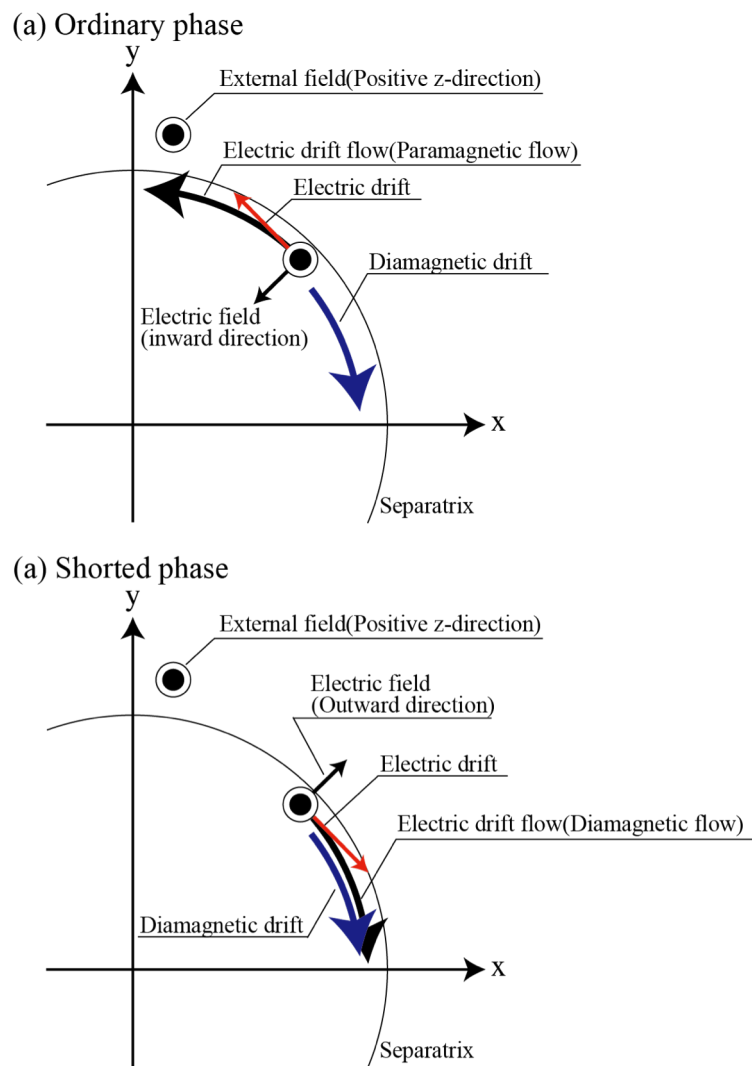


Fig.2.4. The schematic view of plasma flow in (a)ordinary phase and (b) end shorted phase.

### 2.2.3. Poloidal flux decay

This theory has been proposed by Belova et.al. [13] and Toshiki Takahashi [14-15]. Belova et.al. described that particle loss associated with resistive flux decay possibly causes a spin-up for FRC. Since this mechanism only available in the vicinity of separatrix or outside of FRC, it produces a local effect. On the other hand, Toshiki Takahashi has proposed the possible mechanism to rotate the whole FRC plasma inside the separatrix.

Until FRC starts to the elliptical deformation, FRC is supposed to have a circular cross section and has an axisymmetric field. Therefore canonical angular momentum is conserved for every charged particle. The canonical angular momentum is expressed as

$$P_{\theta} = mv_{\theta}r + q\psi(r, z) \quad (33)$$

, where  $\Psi$  is the poloidal flux function. If the canonical angular momentum is conserved, eq.(2-33) becomes

$$m\Delta(v_{\theta}r) + q\Delta\psi = 0 \quad (34)$$

$$m\Delta(v_{\theta}r) = -q\Delta\psi \quad (35)$$

assuming that poloidal flux decay is caused by plasma resistivity and plasma parameters are axisymmetric. Since right term of eq.(2-35) has positive sign when poloidal flux is decreased by the resistivity, the angular momentum of every particle is

increased. In addition to the flux decay, the averaged radius of guiding center is expected to be decreased when the separatrix radius shrinks, resulting in further increase in toroidal flow velocity.

## Reference

- [1] F.C. Jahoda, E.M. Little, W.E. Quinn, F.L. Ribe, G.A. Sawyer, J. Appl. Phys. **35**, 2351(1964)
- [2] E.M. Little, W.E. Quinn, G.A. Sawyer, Phys. Fluids **8**, 1168(1965)
- [3] G.A. Sawyer, V.A. Finlayson, F.C. Jahoda, K.S. Thomas, Phys. Fluids **10**, 1564(1967)
- [4] N.M. Ferraro, Astrophysical journal **662**, 512(2007)
- [5] M. Tuszewski, NUCLEAR FUSION **28**, 11(1988)
- [6] C.E. Seyler, Phys. Fluids **22** 2324(1979)
- [7] R.K. Linford, W.T. Armstrong, D.A. Platts, E.G. Sherwood, Plasma Physics and Controlled Nuclear Fusion Research **2**, 447(1979)
- [8] D.A. Barnes, C.E. Seyler, paper 2C22, presented at Sherwood Mtg., Tucson, AZ, 1980
- [9] D.S. Harned, D.W. Hewett, Nuclear Fusion **24**, 2(1984)
- [10] L. C. Steinhauer, Physics Of Plasmas **9**, 9(2002)
- [11] L. C. Steinhauer, Physics Of Plasmas **15**, 012505(2008)
- [12] L. C. Steinhauer, Phys. Fluids, **24**, 2(1981)
- [13] E.V. Belova, et.al., Nucl. Fusion **46**, 162(2006)
- [14] To. Takahashi, et.al., PFR **2**, 008(2008)
- [15] T. Ikeda, et.al., Proceedings of ITC **18**, (2008)

### 3. Experimental setup

#### 3.1. Overview of NUCTE-III device

This research was carried out on the NUCTE-III device that is a facility of reversed bias theta pinch experiment. The schematic view of NUCTE-III device is shown in fig.3.1. A quartz tube with outer diameter of 256 mm and length of 2 m has been employed as a discharge tube in which two small brunch pipes exist. 32 theta pinch coils are mounted on the quartz discharge tube. In this series of experiment, discharge gas is puffed by electromagnetic valve that is attached on the brunch pipe of discharge tube.

The theta pinch coil has a width of 50 mm and is made of copper. The NUCTE-III device has a lot of flexibility on arrangement of theta pinch coils. In this series of experiment, eight mirror-coils, two tapered-coils and 22 center-coils are mounted in length of about 180 cm. Then measurement space (slit) of 5 mm exists between each theta pinch coil. The center coil has inner diameter of 34 cm and the mirror coil has inner diameter of 32 cm. In addition, tapered coil is set between a center coil and a mirror coil to adjust the different diameters of a center coil and a mirror coil. These theta pinch coils are attached to a collector plate in parallel. The mirror ratio defined as  $R_M=(R_{center}/R_{mirror})^2$  is about 1.1.

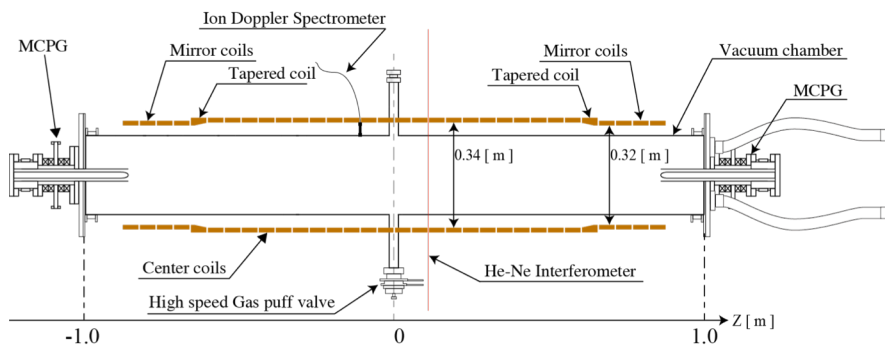


Fig.3.1. The schematic view of the NUCTE-III with plasma guns

The collector plate is connected to capacitor banks which consist of a fast bank with capacitance of  $67.5 \mu\text{F}$ , a pre-ionization bank with  $11.25 \mu\text{F}$  and a slow bank with  $1920 \mu\text{F}$ . The connection between collector plate and the capacitor banks is schematically shown in fig3.2. The characteristic of these banks is summarized in table 3.1. The slow-bank is charged up to  $2.5 \text{ kV}$  to generate a bias field with rise time of  $90 \mu\text{s}$  and field strength of up to  $37.5 \text{ mT}$ . The fast-bank is charged at  $32 \text{ kV}$  to generate a main compression field with rise time of  $4 \mu\text{s}$  and field strength of  $0.5 \text{ T}$ . The decay time of the main compression field is prolonged to  $120 \mu\text{s}$  by a crowbar circuit.

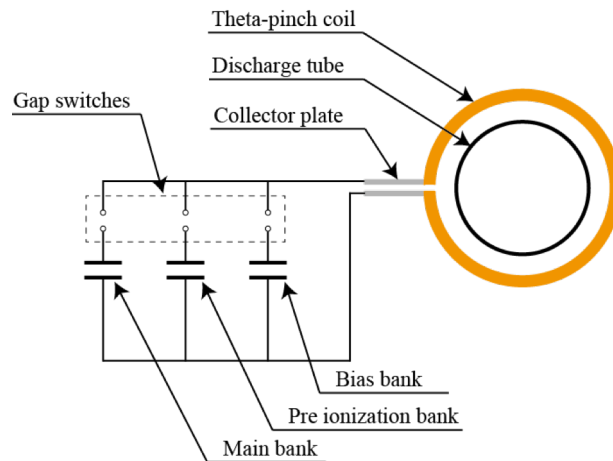


Fig3.2. Connection of collector plate and capacitor banks

Table3.1. The characteristics of fast and slow banks

	Capacitance[ $\mu\text{F}$ ]	$V_{\text{charge}}$ [kV]	Number	Energy [kJ]
Main-field	67.5	32	18	34.6
Pre-ionization	11.25	25	3	3.5
Gus-puff	3.75	20	1	0.8
Bias-field	2000	2-2.5	5	4.0

In this series of experiment, pre-ionization plasma has been generated by large ringing current driven by pre-ionization bank with capacitance of 11.25  $\mu\text{F}$  and charging voltage of 25 kV. The ringing current flows azimuthally on the theta-pinch coils and generates a time varying axial magnetic field inside the discharge tube, which generates an azimuthal electric field to pre-ionize the discharge gas.

### 3.2. Formation scheme of FRC

In the NUCTE-III device, a FRC is generated by FRTP (Field Reversed Theta Pinch) method. A sequence of the FRTP method in the NUCTE-III is illustrated in fig.3.3. (a) The discharge tube is evacuated to about  $2.0 \times 10^{-6}$  Torr by turbo molecular pump. Then a discharge gas of deuterium is puffed by high speed gas-puff valve into the discharge tube. The discharge tube is typically filled with 1.5-2.0 mTorr of deuterium gas.

(b) Bias magnetic field is applied in the discharge tube by the slow bank. Then after discharge gas is filled in the discharge tube, large ringing current is supplied in theta pinch coils to pre-ionize the gas. The bias magnetic flux is frozen in the pre-ionized plasma.

(c) Main compression field which has an opposite polarity of bias magnetic field is applied in the discharge tube when bias magnetic field strength is peaked. The main compression field is ramped up to 0.5 T within a rise time of 3-4  $\mu\text{s}$ . In a radial compression phase, the pre-ionized plasma is compressed and heated by main compression field and azimuthal plasma current is formed in the periphery of the pre-ionized plasma. Then magnetic reconnection takes place at the both ends of the plasma in which magnetic field strength is higher than any other region.

(d) After magnetic reconnection, closed flux region of FRC is established and then axially contracted by a tension of magnetic field line. In this contraction phase, compressional heating also arises and the FRC reaches equilibrium.

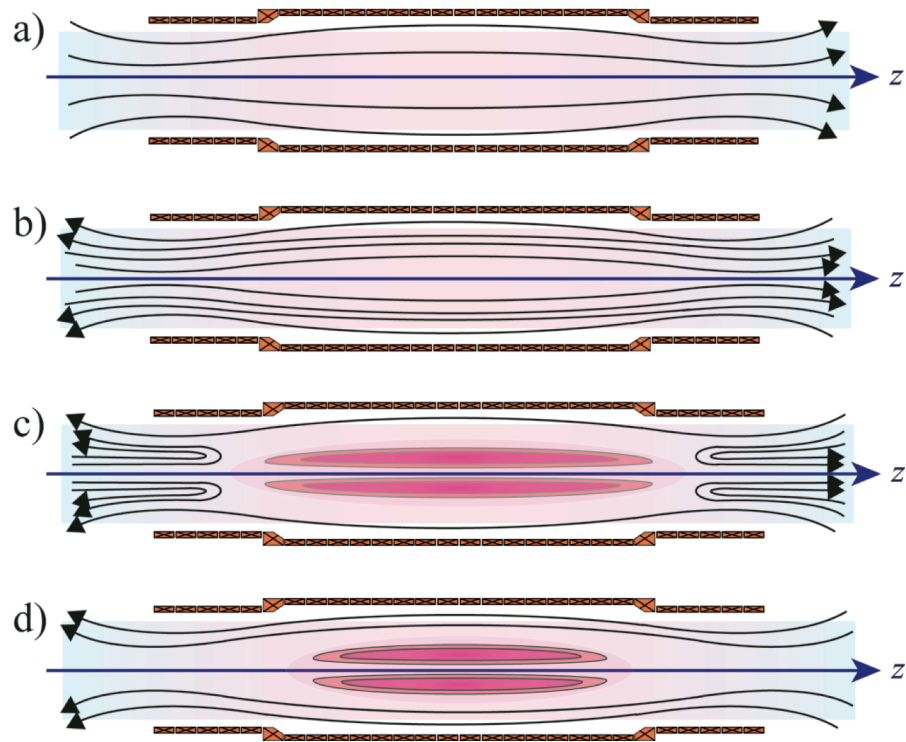


Fig3.3. Formation scheme of FRC by FRTP method

### 3.3. Plasma parameters of FRC

#### 3.3.1 Separatrix radius and separatrix length

FRC's core closed field region is embedded inside an open magnetic field region. A separatrix is defined as a boundary between the open and closed field regions. The FRC's shape is represented by the separatrix radius in  $r$ -direction and the separatrix length in  $z$ -direction. The separatrix radius could be estimated by using axial magnetic field  $B_z$  and axial magnetic flux  $\phi$  measured by magnetic probes and flux loops. The magnetic probes are installed on the surface of discharge tube and flux loop is mounted on the discharge tube. The magnetic flux inside of the theta pinch coil is expressed as

$$\phi = \int B_z dS \quad (1)$$

To calculate the separatrix radius  $r_s$ , vacuum magnetic field and vacuum magnetic flux are defined as  $B_{zv}$  and  $\phi_v$ , respectively. In addition, the magnetic field and the magnetic flux with plasma are defined as  $B_{zp}$  and  $\phi_p$ , respectively. Since the formed FRC has highly elongated separatrix shape, we assume that the axial field in the vacuum region is uniform. Under this assumption,  $\phi_v$  and  $\phi_p$  are represented as

$$\phi_v = \pi r_l^2 B_{zv} \quad (2)$$

$$\phi_p = \pi(r_l^2 - r_s^2)B_{zp}. \quad (3)$$

, where  $r_l$  is a radius of flux loop mounted on the center of the discharge tube.

Therefore the separatrix radius of mid-plane is calculated from eq.(2) and eq.(3) as

$$r_s = r_l \sqrt{1 - \frac{\phi_p B_{zv}}{\phi_v B_{zp}}} . \quad (4)$$

Furthermore, if the FRC's axis is detached from the geometrical axis, the acentric separatrix radius is expressed by using magnetic flux signal of a mid-plane as

$$r_s(z) = r_w(z) \sqrt{1 - \frac{\phi_p B_{zv}}{\phi_v B_{zp}} \frac{1 - \left(\frac{r_s}{r_w(z)}\right)^2}{1 - \left(\frac{r_s}{r_l}\right)^2}} \quad (5)$$

. where  $r_w$  is a radius of theta pinch coil at the  $z$ -position.

The separatrix length is calculated based on  $z$ -distribution of the separatrix radius. The FRC's poloidal cross section could be estimated by reconstructing the  $z$ -distribution of separatrix radius. Since the total number of flux loop and magnetic probe is limited, separatrix radius between measurement locations is interpolated by using a spline function. Note that the assumption that the axial field in the vacuum region is uniform is not valid for both end regions of the FRC plasma where the field line curvature is not negligible. For calculation of separatrix length,  $z_+$  and  $z_-$  are defined as  $z_+$  is the axial position in positive axial direction where the separatrix radius becomes half of the maximum separatrix radius and  $z_-$  for negative axial direction. We define the separatrix length by using use  $z_+$  and  $z_-$  as,

$$l_s = z_+ - z_- . \quad (6)$$

### 3.3.2 Plasma volume

A volume of a FRC is calculated from the  $z$ -distribution of the separatrix radius. A FRC volume is approximated as an ensemble of disks with width of  $dz$  and radius of  $r_s$ . Therefore the volume of FRC is achieved by integration of the volume of each disk from  $z_+$  to  $z_-$  as follows.

$$V_{FRC} = \int_{z_-}^{z_+} \pi r_s^2(z) dz \quad (7)$$

### 3.3.3. Magnetic axis

To derive a radial position of a magnetic axis, we consider the two dimensional equilibrium for FRC. An equation of motion for single fluid is expressed as

$$Mn \frac{d\mathbf{v}}{dt} = \mathbf{J} \times \mathbf{B} - \nabla p \quad (8)$$

, where  $M$  is a mass of ion,  $n$  is a particle density,  $\mathbf{J}$  is a current density and  $p$  is a total pressure of plasma. Furthermore current density is

$$\mathbf{J} = en(\mathbf{v}_i - \mathbf{v}_e). \quad (9)$$

In eq.(8), the terms of time-derivative is zero for consideration of an equilibrium of a FRC. Thus eq.(8) becomes

$$\mathbf{J} \times \mathbf{B} = \nabla p \quad (10)$$

The  $r$ -component of eq.(10) on the mid plane could be described by using the Ampere's law  $\nabla \times \mathbf{B} = \mu_0 \mathbf{J}$  as

$$-\frac{1}{\mu_0} \frac{dB_z}{dr} = \frac{dp}{dr} \quad (11)$$

$$\therefore \frac{d}{dr} \left( p + \frac{B_z^2}{2\mu_0} \right) = 0. \quad (12)$$

Then we can achieve an expression of radial pressure balance to integrate eq.(12) as

$$p + \frac{B_z^2}{2\mu_0} = \frac{B_e^2}{2\mu_0} \equiv p_{ex} (\text{constant}) \quad (13)$$

, where  $B_e$  is an external magnetic field. From this eq.(13)  $B_z$  is described as

$$B_z(r) = \pm \sqrt{2\mu_0(p_{ex} - p)}. \quad (14)$$

From eq.(1), poloidal flux  $\phi$  is expressed as

$$\phi(r) = 2\pi \int_{r'=0}^r r' B_z(r') dr' \quad (15)$$

$$\therefore \frac{d\phi}{dr} = 2\pi r B_z. \quad (16)$$

Substituting the eq.(14) into the eq.(16), we obtain the following expression.

$$\pm \frac{d\phi}{\sqrt{2\mu_0(p_{ex} - p)}} = 2\pi r dr \quad (17)$$

$$\int_{r=0}^R \frac{d\phi}{\sqrt{2\mu_0(p_{ex} - p)}} = 2\pi \int_{r=0}^R r dr \quad (18)$$

$$- \int_R^{r_s} \frac{d\phi}{\sqrt{2\mu_0(p_{ex} - p)}} = 2\pi \int_R^{r_s} r dr \quad (19)$$

Since pressure is a surface function of  $\phi$  and  $\phi$  becomes 0 at  $r=0$  and  $r=r_s$ , eq.(18) and eq.(19) has same value. Therefore following expression is achieved by equating the eq.(18) and the eq.(19).

$$\int_{r=0}^R r dr = \int_R^{r_s} r dr \quad (20)$$

$$\therefore R = \frac{r_s}{\sqrt{2}} \quad (21)$$

### 3.3.4. Plasma beta

A beta is an indicative value of magnetic confinement plasma. In this section, the beta value is calculated in a case of equilibrium phase of FRC. By an expression of axial force balance, following expression is obtained.

$$\nabla \cdot \vec{P} = -\nabla \cdot \overleftarrow{T}^m \quad (22)$$

$$\int_V (\nabla \cdot \vec{P})_z dV = - \int_V (\nabla \cdot \overleftarrow{T}^m)_z dV \quad (23)$$

, where  $\vec{P}$  and  $\overleftarrow{T}^m$  are pressure tensor and magnetic pressure tensor, respectively. By applying a Gauss's low for eq.(23), eq.(23) is expressed as

$$\int_S (\vec{P})_z dS = - \int_S (\overleftarrow{T}^m)_z dS. \quad (24)$$

Assuming that plasma does not exist at locations much far away from a FRC or outside of separatrix radius, eq.(24) could be expanded as

$$\begin{aligned} \int_0^{r_s} P dS|_{z=0} & \quad (25) \\ & = - \int_0^{r_s} \frac{B_z^2}{2\mu_0} dS|_{z=0} \\ & \quad - \int_{r_s}^{r_w} \frac{B_e^2}{2\mu_0} dS|_{z=0} + \int_0^{r_w} \frac{B_e^2}{2\mu_0} dS|_{z=\infty}. \end{aligned}$$

Moreover since magnetic flux formed by external field is conserved inside the coil, following expressions hold as

$$\int_{r_s}^{r_w} B_e 2\pi r dr = \int_0^{r_w} B_0 2\pi r dr \quad (26)$$

$$B_0 = B_e \left( 1 - \frac{r_s^2}{r_w^2} \right) \quad (27)$$

$$B_0 = B_e(1 - x_s^2), x_s \equiv \frac{r_s}{r_w}. \quad (28)$$

Then eq.(25) is rearranged by substituting eq.(13) and eq.(27) as follows

$$\int_0^{r_s} p r dr = \frac{B_e^2}{4\mu_0} r_s^2 \left(1 - \frac{1}{2} x_s^2\right) \quad (29)$$

$$\frac{\int_S \left( \frac{p}{\frac{B_e^2}{2\mu_0}} \right) dS}{\pi r_s^2} = 1 - \frac{1}{2} x_s^2 \quad (30)$$

$$\langle \beta \rangle = \frac{\int_S \beta dS}{\pi r_s^2} = 1 - \frac{1}{2} x_s^2, \beta = \frac{p}{\frac{B_e^2}{2\mu_0}}. \quad (31)$$

Therefore averaged beta value is related to  $x_s$ . Since the beta is expressed as a ratio of plasma thermal pressure and magnetic pressure, the beta indicates confinement efficiency for magnetic confinement plasma. If plasma has a higher beta value, the plasma thermal pressure is sustained by smaller magnetic field.

### 3.3.5. Poloidal flux

In this section, we calculate a poloidal flux remained in a FRC. A FRC in equilibrium phase is usually described by RRP (Rigid Rotor Profile) model in which a FRC rotates as rigid rotation and angular frequency is same at each radial position. In RRP model, magnetic field profile is expressed as

$$\begin{aligned}
B_z(r) &= B_e \tanh \kappa \left( \frac{r^2}{R^2} - 1 \right), \kappa \\
&\equiv \tanh^{-1} \left\{ \frac{B_z(r_s)}{B_e} \right\}.
\end{aligned} \tag{32}$$

Therefore poloidal flux is expressed by use of eq.(32) as follows

$$\begin{aligned}
\phi_p &= 2 \int_0^{r_s} B_z 2\pi r dr \\
&= 2\pi B_e \int_0^{r_s} r \tanh \kappa \left( \frac{r^2}{R^2} - 1 \right) dr
\end{aligned} \tag{33}$$

Then eq.(33) is normalized with poloidal flux in theta pinch coil as

$$\frac{\phi_p}{\phi_w} = \frac{x_s^2}{\kappa} \log(\cosh \kappa). \tag{34}$$

In addition, eq.(34) could be approximated as

$$\phi_p \cong \frac{\sqrt{3}}{2\sqrt{2}} x_s^3 \phi_w. \tag{35}$$

### 3.3.6. Total temperature

In the thermal equilibrium plasma thermal pressure is expressed as

$$p = n_e k_B T \tag{36}$$

, where  $T$  is a total temperature ( $T=T_e+T_i$ ). By use of eq.(36), beta could be rewritten

$$\beta = \frac{2\mu_0 n_e k_B T}{B_e^2}. \quad (37)$$

Thus total temperature is derived as

$$T[\text{eV}] = \frac{B_e^2}{2\mu_0 n_e e} \left(1 - \frac{1}{2} x_s^2\right). \quad (38)$$

### 3.3.7. The value of $\bar{s}$

In the theoretical research of FRC, kinetic effect of ion is often focused because of the high-beta characteristic of a FRC. The kinetic effect is approximately characterized by the number of ion Larmor-radius between  $R$  and  $r_s$ . Then the  $\bar{s}$  is expressed as

$$\bar{s} = \int_R^{r_s} \frac{r}{r_s \rho_i} dr \quad (39)$$

, where  $\rho_i$  is a ion gyro radius. Additionally the value of  $\bar{s}$  is obtained by experimentally as follows

$$\bar{s} = \frac{\phi_p}{2\pi r_s \rho_i B_e} \quad (40)$$

$$\rho_i = \frac{1}{\omega_{ci}} \sqrt{\frac{T_i}{m_i}} = \frac{\sqrt{m_i T_i}}{e B_e}. \quad (41)$$

### 3.4. Measurement system

#### 3.4.1 Magnetic field and flux diagnostics

As described in Sec 3.3.1, axial magnetic field and axial flux measurements are required to reconstruct FRC's shape as axial profile of separatrix radius. To measure the magnetic field and magnetic flux we have used magnetic probes and flux-loops, respectively. The flux loop is a one-turn loop coil wound on the discharge tube, and it measures the time derivative of the magnetic flux penetrating the surface of the flux loop. Output voltage of the flux loop is given by using Stokes' law as follows

$$\begin{aligned}\nabla \times \mathbf{E} &= -\frac{\partial \mathbf{B}}{\partial t} \\ \int_S (\nabla \times \mathbf{E}) \cdot d\mathbf{S} &= -\frac{\partial}{\partial t} \int_S \mathbf{B} \cdot d\mathbf{S} \\ \oint_{loop} \mathbf{E} \cdot d\mathbf{l} &= -\frac{\partial \Phi}{\partial t} \\ V_{loop} &= -\frac{\partial \Phi}{\partial t}\end{aligned}\tag{42}$$

, Where  $\mathbf{E}$  is an electric field induced along a flux loop,  $\mathbf{B}$  is a magnetic field penetrating on flux loop surface,  $\Phi$  is a magnetic flux on the surface of flux loop, and  $V_{loop}$  is an induced voltage along a flux loop.

The magnetic probe is a small coil, and its output voltage is given by same calculation of the flux loop. The output voltage  $V_{probe}$  is expressed as

$$V_{probe} = -NS \frac{\partial B}{\partial t}\tag{43}$$

,where  $N$  is a turn number of magnetic probe and  $S$  is an area of probe surface. Since

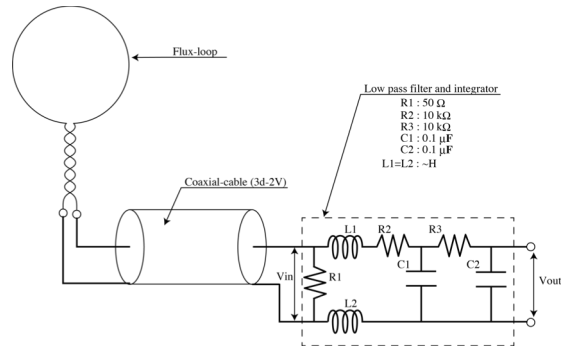


Fig.3.4. Circuit diagram of flux loop with integrator

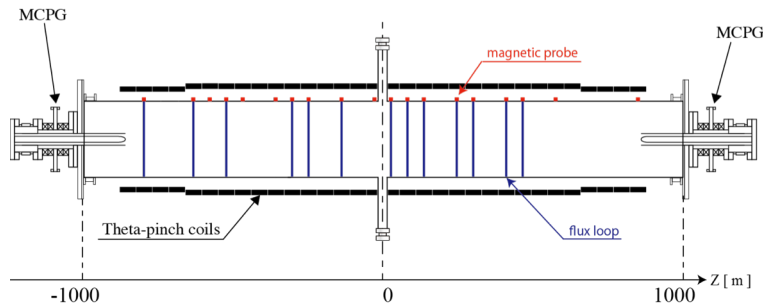


Fig.3.5. Positions of magnetic-probes (red squares) and flux-loops (blue lines)

output voltage of magnetic probe and magnetic flux is proportional to time derivative of magnetic flux, the output signal is required to be integrated with time to achieve magnetic field and magnetic flux signals. Integration circuits have been used to integrate the raw output signals of magnetic probes and flux loops. The integration circuit attached to flux loop is illustrated in fig.3.4. It consists of low pass filter and integrator. The low pass filter has  $0.1 \mu\text{s}$  of time constant and the integrator has  $1 \text{ ms}$  of time constant, which is much longer than the period of the target phenomena of  $<100 \mu\text{s}$ .

In this research, 19 magnetic probes and 13 flux loops are equipped on a discharge tube. The position of magnetic probes and flux loops are indicated in fig.3.5 and summarized in table 3.2.

Table 3.2. Axial locations of magnetic probes and flux loops

No.	Magnetic probe [ cm ]	Flux loop [ cm ]
1	85.3	45.8
2	57.8	40.3
3	46.8	29.3
4	41.3	23.8
5	30.3	12.8
6	24.8	7.3
7	13.8	1.8
8	8.3	-14.7
9	2.8	-25.7
10	-2.7	-31.2
11	-13.7	-53.2
12	-24.7	-64.2
13	-30.2	-80.7
14	-35.7	
15	-46.7	
16	-52.2	
17	-57.7	
18	-63.2	
19	-79.7	

### 3.4.2 Emission measurement by photo multiplier tube

A PMT (Photo Multiplier Tube) amplifies weak light signal by photoelectric effect. In this research, 60 channels of optical measurement system are employed to measure emission from FRC plasma. Each one channel of this system consists of a collimator, an optical fiber, an interference filter, a PMT, and an AD-converter as shown in fig.3.6. The collimator located outside of the quartz discharge tube collimates emission light from FRC plasma. Fig.3.7 shows a diagram of the collimators. Plano-convex lenses are made of synthetic silica with a focal length of 30 mm and 100 mm. The plano-convex lens collimates an emission of plasma and focuses the light onto the

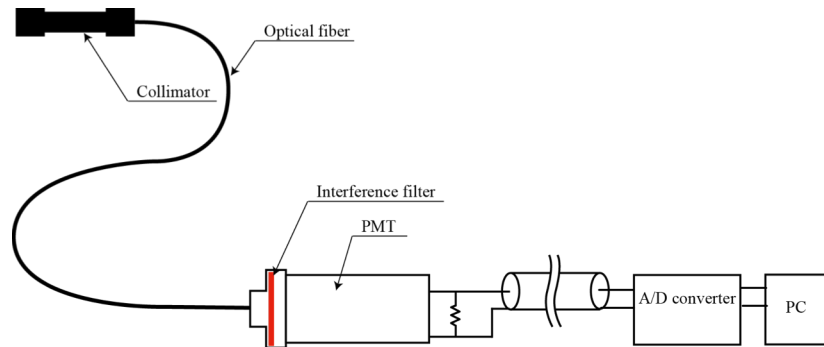


Fig.3.6. Optical measurement system used by PMT

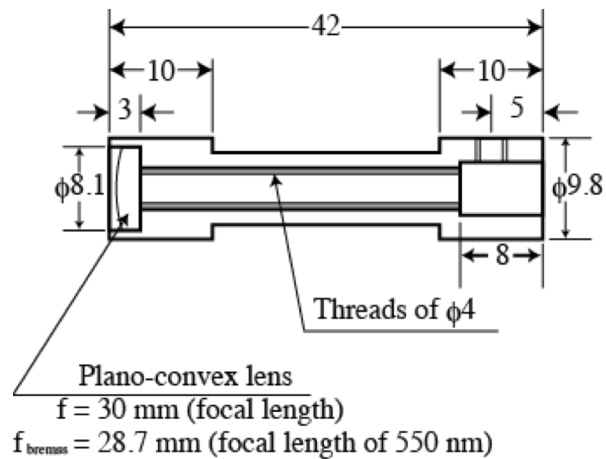


Fig.3.7 The schematic view of collimator

optical fiber end. Additionally, threads are arranged on the interior wall to block a stray light. This collimator system has  $\phi 6$  mm of spatial resolution on the center of discharge tube. An optical signal observed by the collimator is transmitted by an optical fiber, and the optical signal is introduced to a PMT which converts the light to an current signal. Finally the output current signal of the PMT is converted to voltage signal by a road resister, and the voltage signal is also converted to digital signal by an A/D convertor. In this research, observed wavelength was selected by switching band pass interference filters. The band pass interference filters with a central wavelength of 270 nm, 656 nm, and 470 nm and bandwidth of 10 nm were used to measure an emission of CV (227.09 nm),  $D_{\alpha}$  (656.10 nm), and HeII (468.58 nm), respectively. A band pass interference filter with a central wavelength of 550 nm and a bandwidth of 10 nm was also employed to measure bremsstrahlung emissions excluding line spectra of deuterium and major impurities. The bremsstrahlung has a wavelength dependence as

$$I(\lambda)d\lambda \propto n_e^2 Z_{eff} T_e^{-\frac{1}{2}} \exp\left(-\frac{hc}{\lambda T_e}\right) \bar{g}_s d\lambda \quad (44)$$

,where  $n_e$  is the electron density,  $Z_{eff}$  is the effective charge number,  $T_e$  is the electron temperature,  $h$  is the Planck's constant,  $c$  is the velocity of light,  $\lambda$  is the wavelength, and  $\bar{g}_s$  is the Gaunt factor. In the condition of this experiment, the exponential term of eq.(44) is approximately unity. Thus eq.(44) becomes

$$I(\lambda)d\lambda \propto n_e^2 Z_{eff} T_e^{-\frac{1}{2}} \frac{c}{\lambda^2} \bar{g}_s. \quad (45)$$

Therefore the bremsstrahlung emission is proportional to the square of electron density assuming uniform electron temperature distribution. Table 3.3 summarizes the sets of

target lines and band pass interference filters.

Table 3.3 Interference filters and corresponding lines of spectra

Target	Observed wavelength of plasma emission	Central wavelength of	bandwidth
C V	227.09 nm	220 nm	10 nm
He II	468.58 nm	470 nm	10 nm
Bremss	550 nm	550 nm	10 nm
D <sub>α</sub>	656.10 nm	650 nm	10 nm

### 3.4.3 He-Ne laser interferometer

An interferometer using Helium-Neon laser system has been used to observe a line-integrated electron density of FRC plasma. The interferometer uses a heterodyne interferometry technique. There are two modes, O-mode and X-mode, when the electromagnetic wave propagates inside plasma with an angle of  $\theta$  from the direction of magnetic field. The refractive index of O-mode wave does not depend on magnetic field and propagating-angle of the wave assuming the frequency of the wave is much higher than electron collision frequency of the plasma. Therefore an electron density of plasma could be measured by choosing a microwave ~ infrared light as a probe laser beam. In this condition, a refractive index  $N$  in plasma is expressed as

$$N = \sqrt{1 - \frac{\omega_{pe}^2(r)}{\omega^2}} = \sqrt{1 - \frac{n_e(r)}{n_c}}, \quad (46)$$

$$n_c \equiv \frac{\epsilon_0 m_e \omega^2}{e^2} \quad (47)$$

,where  $\omega_{pe}$  is a plasma frequency,  $\omega$  is an angular frequency of an electromagnetic wave propagating in plasma and  $n_c$  is the cut-off density. The  $n_c$  is calculated as follows

$$n_c = \frac{1.12 \times 10^{15}}{\lambda^2}, \quad (48)$$

,where  $\lambda$  is a vacuum wavelength of an electromagnetic wave. Then we consider the condition that an electromagnetic wave with wavelength of  $\lambda$  is injected along a center of plasma mid-plane as described in fig.3.8. In this condition, phase change of the electromagnetic wave is expressed as

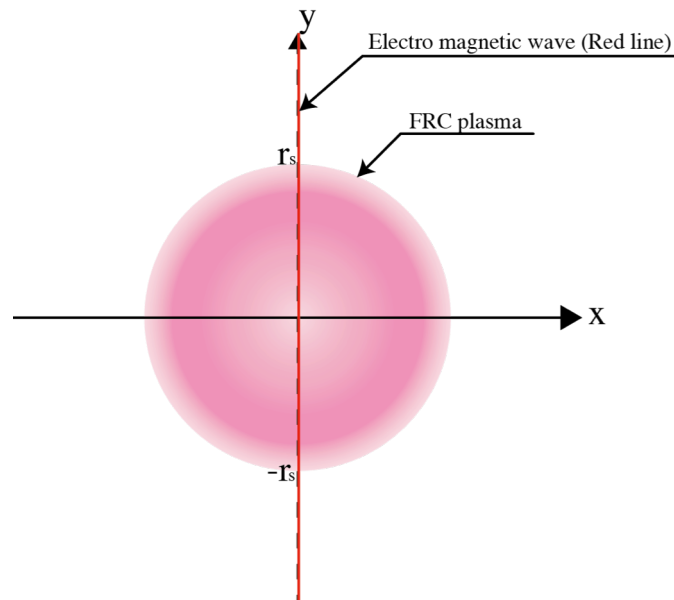


Fig.3.8 A schematic view of propagating electromagnetic wave in FRC

$$\begin{aligned}\phi &= \int_{-r_s}^{r_s} (k_0 - k_p) dr \\ &= \frac{2\pi}{\lambda} \int_{-r_s}^{r_s} (1 - N) dr,\end{aligned}\quad (49)$$

,where  $k_0$  and  $k_p$  are wave numbers in vacuum and in plasma, respectively. By using eq.(46), the phase change of eq.(49) is expressed as

$$\phi(r) = \frac{2\pi}{\lambda} \int_{-r_s}^{r_s} \left( 1 - \sqrt{1 - \frac{n_e(r)}{n_c}} \right) dr. \quad (50)$$

Here,  $n_c$  is much higher than  $n_e$  of FRC since typical electron density is  $10^{21} \sim 10^{22} \text{ m}^{-3}$  in this series of experiment. Therefore the second term in the integral of eq.(50) could be expanded by Taylor expansion. Then eq.(50) becomes

$$\begin{aligned}\phi(r) &\cong \frac{2\pi}{\lambda} \int_{-r_s}^{r_s} \frac{n_e(r)}{2n_c} dr \\ &= \frac{\pi e^2}{m\varepsilon_0 \omega^2 \lambda} \int_{-r_s}^{r_s} n_e(r) dr.\end{aligned}\quad (51)$$

By using the eq.(51), line integrated electron density is calculated as

$$\begin{aligned}\int_{-r_s}^{r_s} n_e(r) dr &= \frac{4\pi\varepsilon_0 m c^2}{e^2 \lambda} \phi(r) \\ &\cong \frac{3.6 \times 10^{14}}{\lambda} \phi(r).\end{aligned}\quad (52)$$

For the measurement of electron density, heterodyne type interferometer is used in this experiment as shown in fig.3.9. In the system He-Ne laser beam with  $3.39 \mu\text{m}$  of wavelength is used as a probe laser beam. Since cut-off density for the He-Ne laser is  $9.8 \times 10^{25} \text{ m}^{-3}$ , line integrated electron density is calculated by eq.(52) as

$$\int_{-r_s}^{r_s} n_e(r) dr \cong 1.1 \times 10^{20} \times \phi(r). \quad (53)$$

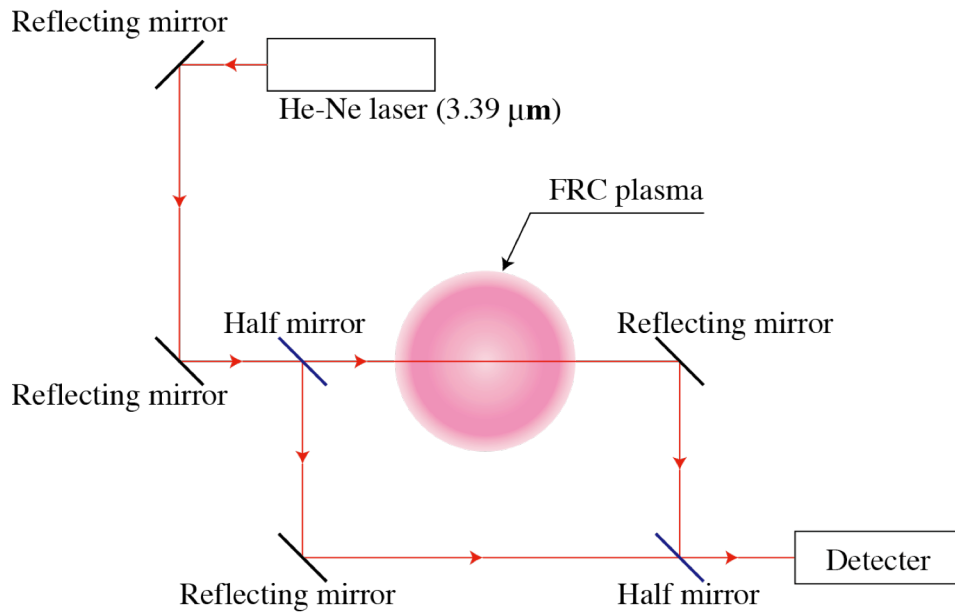


Fig.3.9. A diagram of an interferometer by using a He-Ne laser

### 3.4.4 Doppler spectroscopy

A Doppler broadening appears on a line emission spectrum from plasma particles when they have a Maxwell-boltzmann type velocity distribution. The Maxwell-boltzmann distribution function is expressed as

$$f(v) = \sqrt{\frac{m}{2\pi kT}} \exp\left(-\frac{mv^2}{kT}\right) dv \quad (54)$$

, where  $m$  is a particle mass,  $T$  is a temperature and  $v$  is a velocity of a particle. An emission from particles with temperature  $T$  is expressed by eq.(54)

$$I_D(\omega)d\omega = \sqrt{\frac{mc^2}{2\pi kT}} \exp\left\{-\frac{mc}{2\omega_0}(\omega - \omega_0)\right\} d\omega \quad (55)$$

, where  $\omega$  is an angular frequency of emission and a  $\omega_0$  is a angular frequency emitted from the quiescent particles. From this equation, FWHM (Full Width at Half Maximum) is calculated as

$$\Delta\lambda_{FWHM} = 7.7 \times 10^{-5} \lambda_0 \sqrt{\frac{T}{A}} \quad (56)$$

, where  $A$  is a mass number. Thus ion temperature  $T_i$  is derived by using eq.(56) as

$$T_i = 1.69 \times 10^8 \text{A} \left( \frac{\Delta \lambda_{FWHM}}{\lambda_0} \right)^2 \text{ [eV]}. \quad (57)$$

In addition, an ion flow velocity is calculated from the peak wavelength of the spectral line  $\lambda_{peak}$  as

$$v_{flow} = \frac{\lambda_{peak} - \lambda_0}{\lambda_0} c. \quad (58)$$

For the Doppler spectroscopy, multichannel spectrometer was employed. Figure 3.10 shows a schematic diagram of the multichannel spectrometer, which consists of a collimator, a Czerny-Turner type monochromator, a cylindrical lens and 16-channel photo multiplier tube array. An emission of FRC is collimated by a collimator and is transmitted through an optical fiber to a monochromator. Then dispersed light from the exit slit of the monochromator is magnified in the wavelength direction by a cylindrical lens and focused on the surface of a 16 channel PMT. Since the

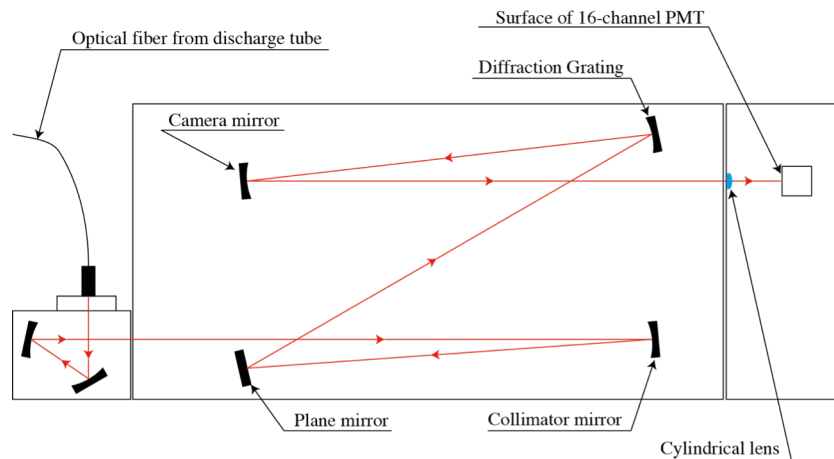


Fig.3.10. The schematic view of a polychromator system

spectrometer has instrumental broadening, calibration is required to achieve accurate ion temperature and flow velocity. Thus calibration test was carried out to measure the instrumental broadening of the spectrometer. The setup is illustrated in fig.3.11. In the calibration test, a low temperature mercury lamp was used as a light source. The Hg I spectrum line of 253.65 nm was selected because C V (227.09 nm) was used to measure an ion temperature and flow velocity of the FRC. In the result of the calibration test, the instrumental broadening was 0.031 nm and channel-width was 0.011 nm. The experimental result in calibration test is shown in fig.3.12. The instrumental broadening of 0.031 nm corresponds to the carbon ion temperature of 38 eV.

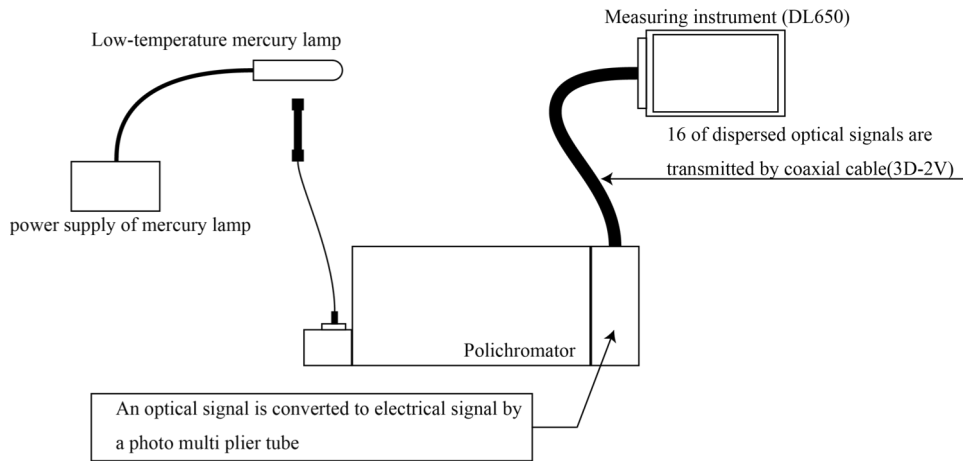


Fig.3.11 The setup diagram of a calibration test

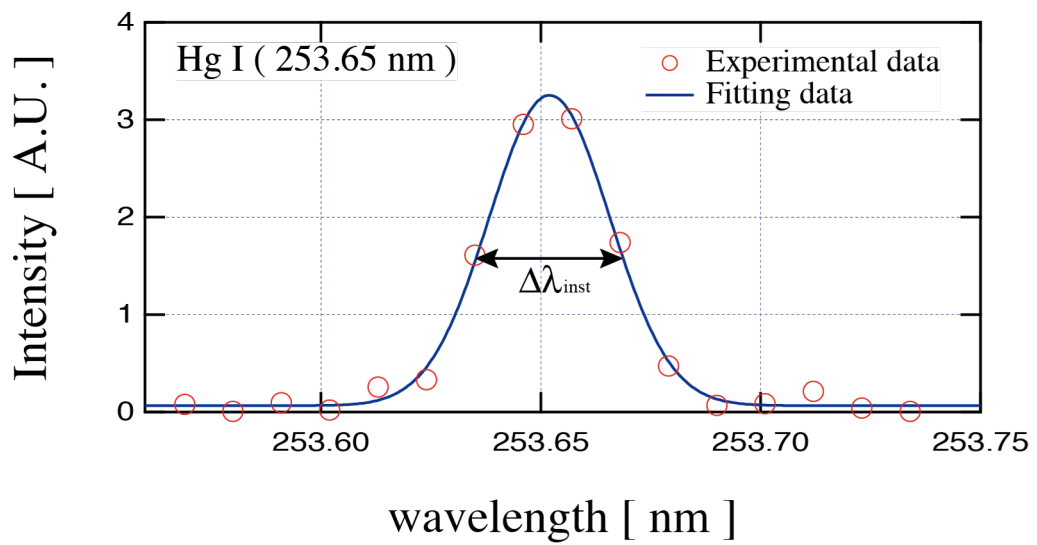


Fig.3.12 Measured instrumental broadening with Hg I of 253.65 nm

## 4. Development of MCPG

### 4.1. Formation scheme of magnetized plasmoid

Discharge and plasmoid formation scheme is illustrated in fig4.1. First, bias magnetic field is applied in MCPG discharge region, and discharge gas is puffed into a gap between inner electrode and outer electrode when bias magnetic field penetrates enough in MCPG. Then high-voltage is added between inner electrode and outer electrode to breakdown the discharge gas. When plasma is formed in a gap, discharge current flows through the electrodes and the discharge current pass through the plasma along  $r$ -direction. The discharge current induces an azimuthal magnetic field, and resulting axially-directed Lorentz-force. Then the plasma is axially accelerated and

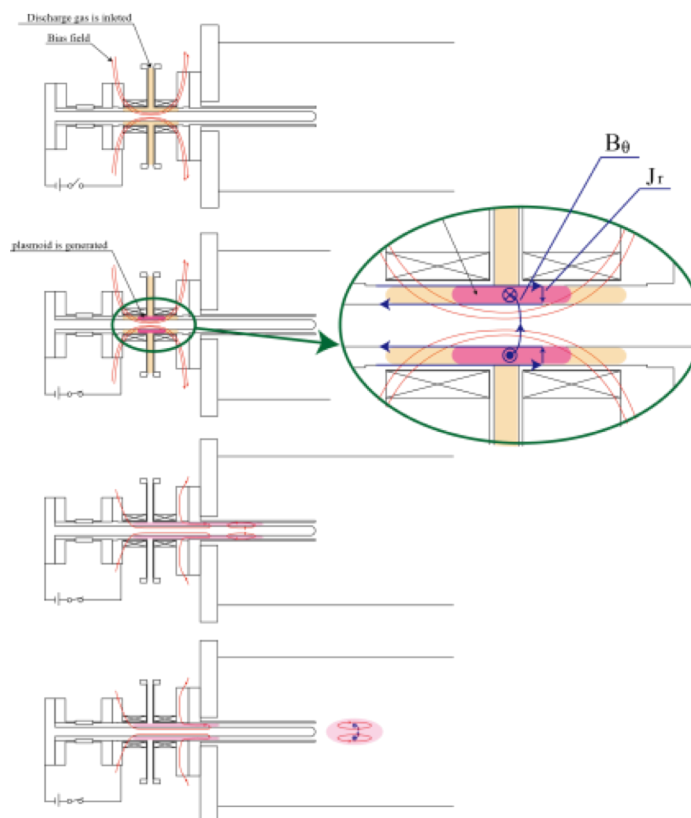


Fig.4.1. A schematic diagram of magnetized plasmoid formation

ejected from the MCPG. Since the plasma traverses bias magnetic field of  $r$ -direction when the plasma is ejected, toroidal current is induced in the plasma. Since discharge current continues to flow along a magnetic field line of bias field, toroidal field is formed in the plasma. Finally magnetic reconnection event occurs in the vicinity of the MCPG muzzle, and spheromak-like plasmoid with both poloidal and toroidal magnetic fields is formed.

#### 4.2. Characteristic of MCPG mounted on the NUCTE

In this research, two MCPGs were used to generate a magnetized plasmoid. The MCPG consists of inner electrode and outer electrode, acceleration electrode and a bias-coil with a turn of 16 as shown in fig4.2. The MCPGs have a length of 465 mm, a bore of 29 mm and a gap between inner and outer electrode of 6.5 cm. The inner electrode is made of tungsten to prevent an impurity originated from electrode from injecting into target plasma. The acceleration electrode has a length of 217.5 mm and is made of copper. It is jugged into the discharge tube (the electrode end locates at  $z =$

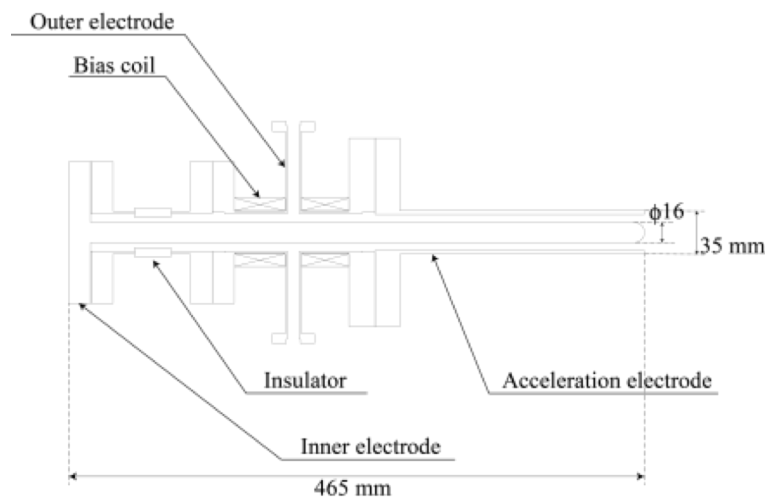


Fig.4.2 Schematic view of MCPG used in this research

85 cm @up, and  $z = -85$  cm @down). Since mirror coil is mounted on  $z = 66.2 \sim 87.7$  cm and  $-66.2 \sim -87.7$  cm, the gun muzzle is under the mirror coil and the ejected plasmoid from MCPG could pass through the mirror region easily.

The MCPG was connected to capacitor and ignitron switch as shown in fig4.3. The capacitor has a capacitance of  $250 \mu\text{F}$  and is charged up to 6 kV. Thus total discharge energy of the MCPG has a 4.5 kJ at a charging voltage of 6 kV. The inductance per unit length of MCPG is estimated by following expression:

$$L_{gun} = \frac{\mu_0}{2\pi} \log\left(\frac{b}{a}\right) \text{ [H/m]} \quad (1)$$

, where  $b$  is an inner radius of outer electrode and  $a$  is an outer radius of inner electrode. Then an inductance of the MCPG is estimated as  $0.13 \mu\text{H/m}$ .

The MCPG has a bias coil with 15 turns which generates a magnetic flux of up to  $0.25 \text{ mWb}$  with ramp-up time of  $97.5 \mu\text{s}$  inside the MCPG. The bias coil was connected to capacitor bank with capacitance of  $2 \text{ mF}$ . Since a thickness of MCPG is  $3 \text{ mm}$ , a penetration time of magnetic field is  $15.7 \mu\text{s}$ . Therefore  $97.5 \mu\text{s}$  of rise time is enough for the magnetic field to penetrate into MCPG. On the other hand, since the

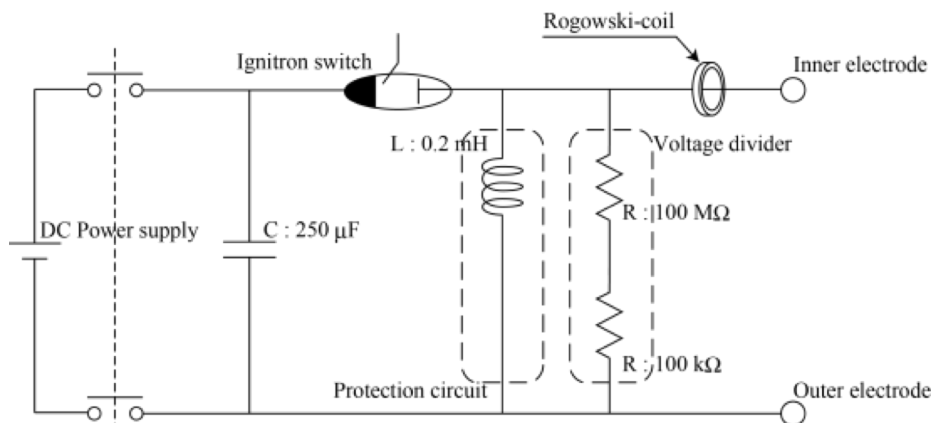


Fig.4.3 Circuit diagram of the MCPG circuit

end flange of the NUCTE has a thickness of 3 cm, the penetration time is 1.6 ms. Thus the bias field could not penetrate into the NUCTE main region. The bias field supplies a poloidal flux of the ejected plasmoid.

#### 4.3. Discharge monitors for MCPG

To observe the MCPG operation, I have measured a bias coil current, a discharge current and a voltage added between inner electrode and outer electrode. A Rogowski coil has been used to measure a time varying current. The output voltage of the Rogowski coil is proportional to time derivative of current. Then the output voltage of the Rogowski coil is expressed as

$$V_{out} = \frac{\mu_0 SN}{l} \frac{dI}{dt} \quad (2)$$

,where  $S$  is a surface of cross section,  $N$  is a turn of the coil,  $l$  is a length of the coil,  $I$  is a current pass through a target. By using a suitable integrator with time constant  $\tau = RC$ , the current is became as follow

$$I = \frac{RC l}{\mu_0 SN} V_{out}. \quad (3)$$

A voltage added the gap of MCPG is measured by a voltage divider. A voltage divider has a simple circuit and consists of various resistors. Then relation between output and input voltage is expressed as

$$V_{out} = \frac{R_1}{R_1 + R_2} V_{in}. \quad (4)$$

In a voltage divider circuit, there are two resistors of  $100 \text{ M}\Omega$  and  $100\text{k}\Omega$ . Thus the ratio of the voltage divider is about  $1/1000$ .

#### 4.4. Magnetic helicity produced by MCPG

A magnetic helicity quantifies a magnetic field structure and has a dimension of energy i.e. magnetized plasmoid has a magnetic helicity because the plasmoid has a toroidal and poloidal field linked each other. Here, let us think a magnetic helicity supplied from a plasma gun. Then a time derivative of the relative helicity is expressed as

$$\frac{dK_R}{dt} = -2 \int_V \mathbf{E} \cdot \mathbf{B} dV - 2 \int_S \phi \mathbf{B} \cdot d\mathbf{S}. \quad (5)$$

In a right hand side of the eq.(5), first term denotes a dissipation term and second term denotes a supply term of a magnetic helicity. When the bounding surface is equipotential,  $\phi$  is constant over it, and the surface integral is vanished. However when the bounding surface has a gap and the gap is electrical insulated, the supply term is expressed as

$$\begin{aligned} \left(\frac{dK_R}{dt}\right)_{supply} &= -2 \left\{ \int_{S_1} \phi \mathbf{B} \cdot d\mathbf{S} \right. \\ &\quad \left. + \int_{S_2} \phi \mathbf{B} \cdot d\mathbf{S} \right\} \end{aligned} \quad (6)$$

$$\left(\frac{dK_R}{dt}\right)_{supply} \quad (7)$$

$$= -2 \left\{ \phi_1 \int_{S_1} \mathbf{B} \cdot d\mathbf{S} + \phi_2 \int_{S_2} \mathbf{B} \cdot d\mathbf{S} \right\}$$

$$\left(\frac{dK_R}{dt}\right)_{supply} = -2 (\phi_2 - \phi_1) \psi \quad (8)$$

,where  $\phi_1$  is an electrical potential of  $S_1$  and  $\phi_2$  is an electrical potential of  $S_2$ . Assuming an inner electrode is regarded as boundary surface  $S_1$  and an outer electrode is regarded as boundary surface  $S_2$ , magnetic helicity injected from MCPG is expressed as

$$\left(\frac{dK_R}{dt}\right)_{inj} = 2V_{gun} \psi_{bias}. \quad (9)$$

## 4.5 Performance test of a plasma gun

### 4.5.1. Typical discharge waveform

In this research, I have focused on energy, magnetic helicity and magnetic field of a magnetized plasmoid generated by the MCPG. Therefore it is important to understand the characteristic of the plasmoid i.e. total inventory, kinetic energy, thermal energy, toroidal field, poloidal field and magnetic helicity.

I have arranged a new test chamber for the MCPG. The test chamber consists of the MCPG and metallic discharge tube with four measurement ports. Generated magnetized plasmoid is ejected from MCPG and travels through the discharge tube.

The MCPG is connected to 250  $\mu\text{F}$  of capacitors and forms a magnetized plasmoid. Figure 4.4 shows a time evolution of discharge current. In the result of discharge current, the half period of discharge is about 60  $\mu\text{s}$  and the peak current is about 30 kA. Thus the supplied electrical energy is 3.2 kJ on each discharge. The peak discharge current depends on electrical energy charged on the capacitor.

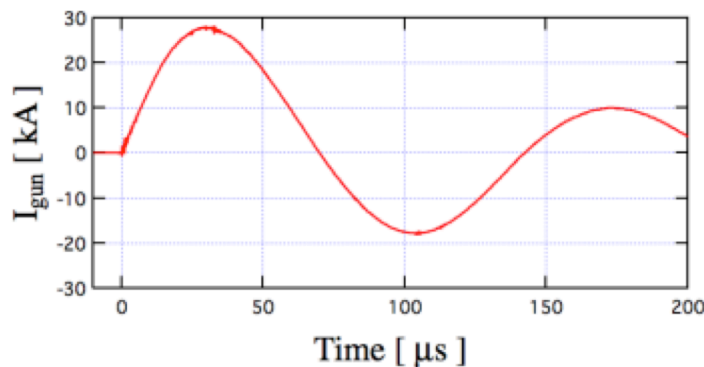


Fig.4.4. Time evolution of gun current

### 4.5.2. Traveling-speed of the plasmoid

The travelling speed of a plasmoid is measured by TOF (Time Of Flight) method in which time difference of rising edge of  $D_{\alpha}$  emission observed at two different

positions. The  $D_\alpha$  emission is measured by a PMT and collimator system that is similar to the emission measurement system for the FRC plasma in the NUCTE. Typical waveform of  $D_\alpha$  emission is shown in fig.4.5. The red line indicates a time evolution of  $D_\alpha$  emission measured at port-1 ( $z = 5$  cm from the MCPG) and the blue-line indicates a  $D_\alpha$  emission measured at port-2 ( $z = 20$  cm from the MCPG). The difference of timing of a rising edge was about  $1.8 \mu\text{s}$  in this condition. Therefore traveling speed is calculated as 83 km/s. Since a magnetized plasmoid is accelerated by a Lorentz-force due to the discharge current and an induced magnetic field, the travelling speed strongly depends on a discharge current. The discharge current increases when the charging voltage of a capacitor is larger. Also the travelling speed depends on an amount of bias magnetic flux. Since the bias magnetic flux has a braking force because of the magnetic pressure, a magnetized plasmoid in MCPG is decelerated by increasing the bias field as shown in fig.4.6. In the fig.4.6, the red circle indicates a travelling speed of the case in which charging voltage is 5 kV and the blue triangle indicates a travel speed of the case in which charging voltage is 6 kV. It is found that a plasmoid have a travelling speed of up to 90 km/s and the speed is decelerated about 20 km/s by the bias field effect.

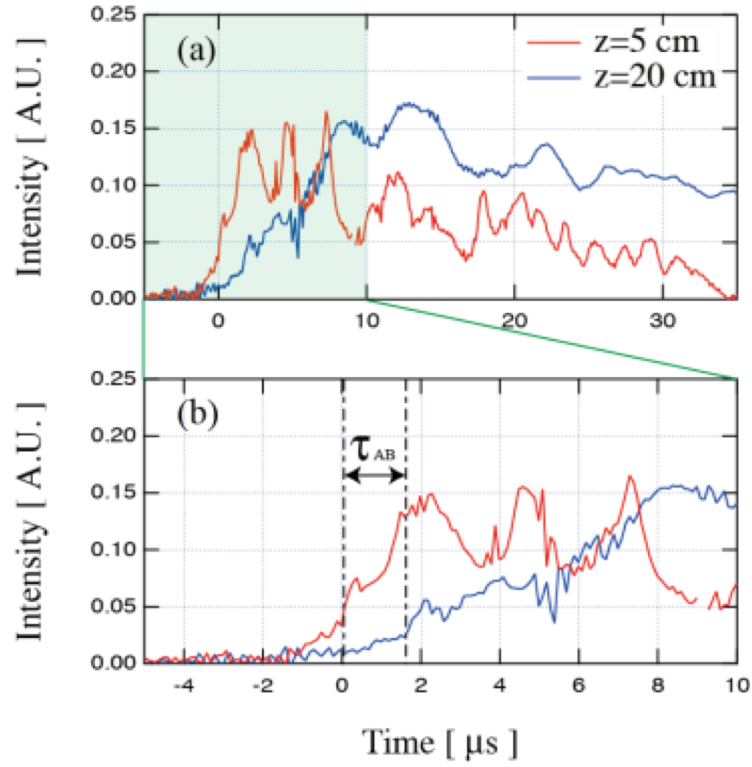


Fig.4.5 A time evolution of spectrum emission of D $\alpha$  is shown in (a). Highlighted region of (a) is expanded as graph (b). Then two dashed vertical lines indicate a rising edge of measured spectrum lines, and the time difference was used to calculate the travelling speed.

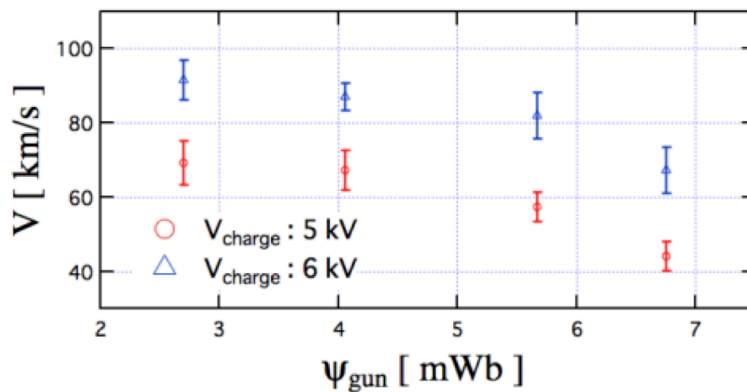


Fig.4.6 Bias flux and charged voltage dependence on travelling speed of the magnetized

#### 4.5.3. Magnetic field measurement of the plasmoid

Since a magnetized plasmoid generated by MCPG has a spheromak-like configuration, the plasmoid has a toroidal field and poloidal field. Internal magnetic field profile was measured by 6 channels magnetic probe array. The magnetic probe has a  $1.0 \times 10^{-5} \text{m}^2$  of cross section and 20 turns, and the magnetic probe is inserted at the port of  $z=5$  cm from the MCPG. Typical waveforms magnetic field is shown in fig.4.7. Although poloidal field has a large strength during early discharge phase (0~20  $\mu\text{s}$ ), it decays faster than the toroidal field. The poloidal field is formed by toroidal current, and the toroidal current is induced when a plasmoid traverse a magnetic field line. Therefore since a plasmoid traverses the bias magnetic field line with higher speed in the early phase, poloidal field strength is higher in early phase and it decays later. On the other hand, toroidal field strength has a slow rise time and slow decay. This is because toroidal field is formed by discharge current pass through a magnetic field line and the discharge current is maintained during the discharge period.

By using multi-channel magnetic probe, magnetic field profile of the magnetized plasmoid was achieved as shown in fig.4.8. The magnetic field profile was achieved at the time of 10  $\mu\text{s}$  from at the discharge. The toroidal field profile shows reversal around the geometrical axis ( $r = 0$  cm) and peaks at  $r = 2\sim 3$  cm. The poloidal field profile shows reversal at the edge of the plasma and peaks at the geometrical axis. These results indicate that the magnetized plasmoid has a spheromak-like field structure with a certain amount of magnetic helicity. The internal field profile is also used to derive the poloidal and toroidal fluxes contained in the magnetized plasmoid.

It is considered that the contained magnetic fluxes depend on a charged voltage and bias magnetic flux of MCPG. Figure 4.9 shows the contained poloidal and toroidal magnetic fluxes as functions of charging voltage of MCPG for three different bias flux of (a) 0.41 mWb, (b) 0.54 mWb, and (c) 0.68 mWb. In all cases, the contained poloidal flux tends to increase gently with increasing the charging voltage and the contained toroidal flux increment is more significant than that of the poloidal flux. These trends are shown as 2D contour maps on bias magnetic flux and charged voltage as shown in fig.4.10. The contour map of poloidal flux is shown in (a) and the contour map of toroidal flux is shown in (b).

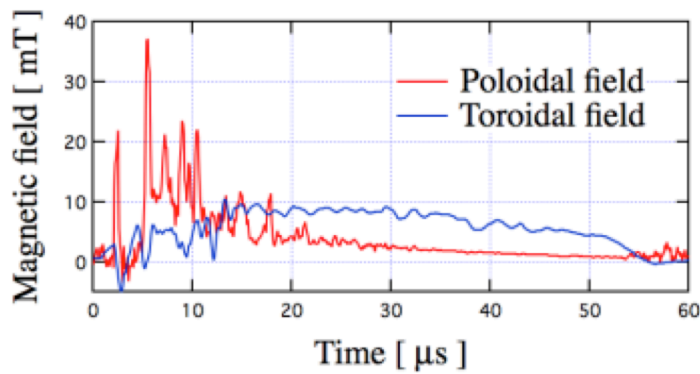


Fig.4.7 Time evolution of magnetic field at the position of peak value

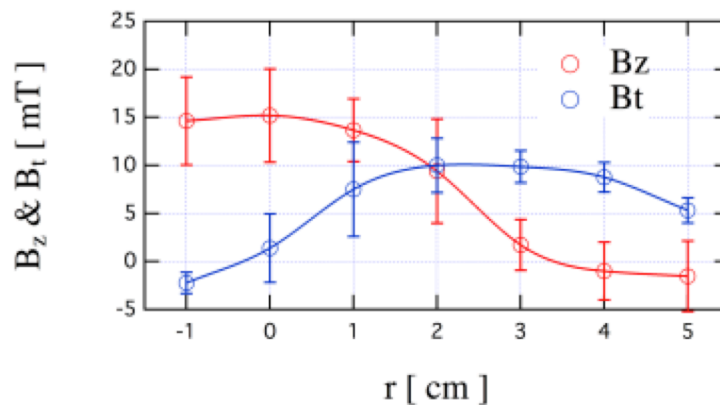


Fig.4.8 Magnetic field profile of the plasmoid

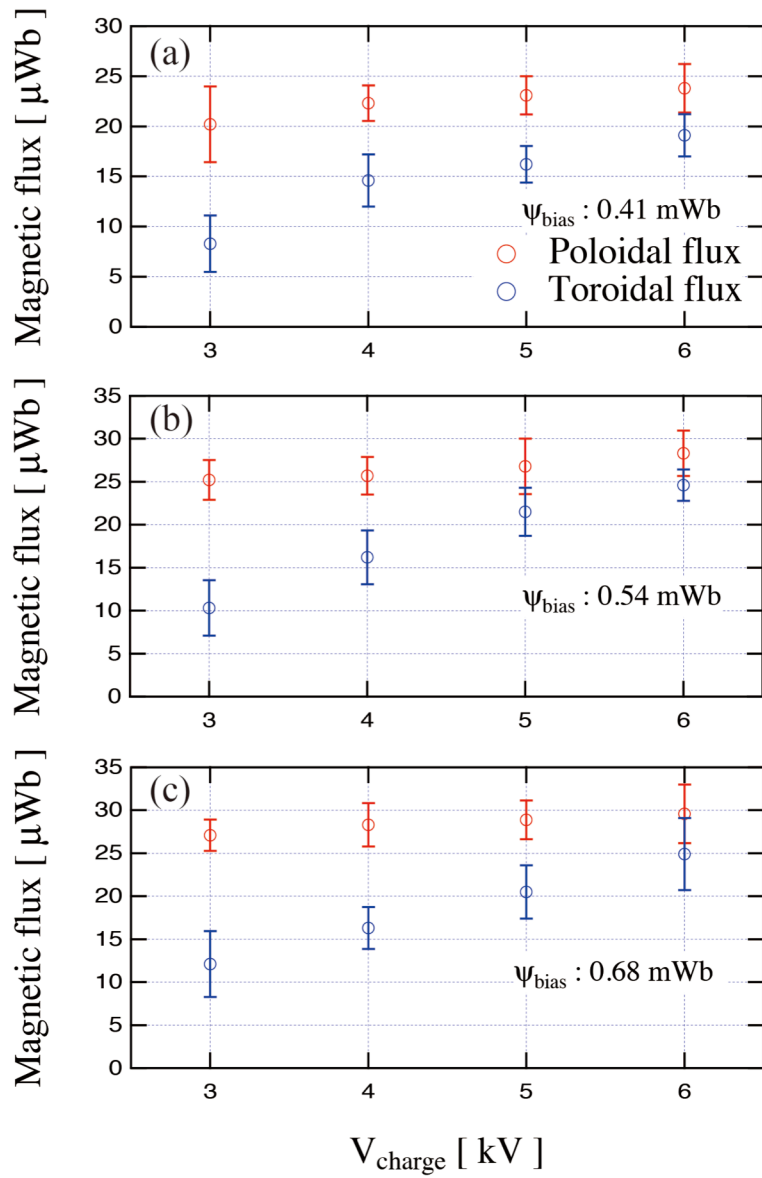


Fig.4.9  $V_{\text{charge}}$  dependence of magnetic flux in the case of (a) bias flux of 0.41 mWb, (b) 0.54 mWb and (c) 0.68 mWb

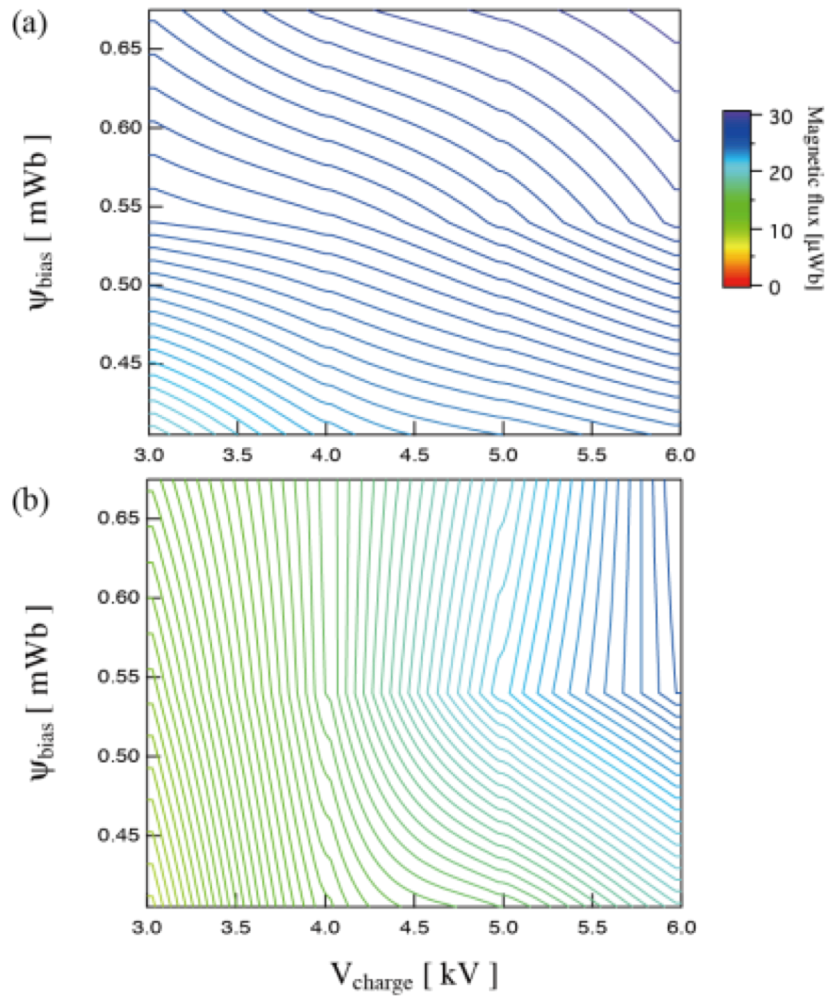


Fig.4.10 Contour plot of poloidal and toroidal flux as functions of bias flux and charging voltage

## 5. Results from single plasmoid injection experiment

### 5.1. Single plasmoid injection for FRC

As described in Section 3.1, two MCPGs were manufactured and installed on the both ends of the NUCTE-III device. This setup conflicts with the axial translation technique of a FRC plasma, which is considered essential to sustain a hot FRC plasma for an long period by using additional heating methods. From the viewpoint of the FRC translation, single side injection of magnetized plasmoid has better compatibility than the double side injection scheme . In this section, evaluation of stabilization effect by single side plasmoid injection is described. The experiment of single side injection was carried out in the NUCTE-III with two MCPGs equipped on the both ends as shown in fig.3.5.

### 5.2. Experimental results of single side injection

The decay time of FRC is evaluated as an e-folding time of the separatrix radius on the mid plane. The observed decay time for FRCs with and without single side plasmoid injection is shown in fig.5.1. Although the decay time of FRC without injection stays in a range of 45 – 55  $\mu\text{s}$ , the decay time of plasmoid-injected FRC scatters widely in a range of 40 – 65  $\mu\text{s}$ . In other words, the single side injection

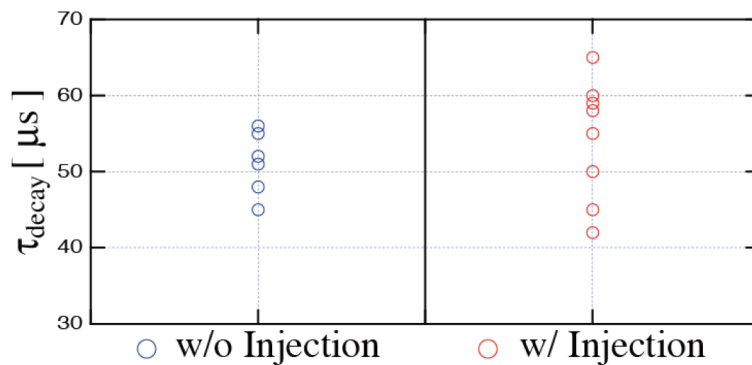


Fig.5.1. The decay time of FRCs with/without magnetized plasmoid injection

sometimes yields positive effect on global FRC sustainment and sometimes negative. Figure 5.2 shows characteristic parameters of rotational instability observed in the FRC with/without single side injection. Figure 5.2 (a) shows the onset time, (b) shows a rotation period and (c) shows a growth time of the rotational instability. It can be said that the single side injection generally suppresses the rotational instability because the averaged parameters of onset time, rotation period and growth time are prolonged. However, the standard deviations shown as error bars in fig. 5.2 also increase when the single side injection was performed. There are some cases in which the rotation speed and the growth rate are enhanced by the plasmoid injection.

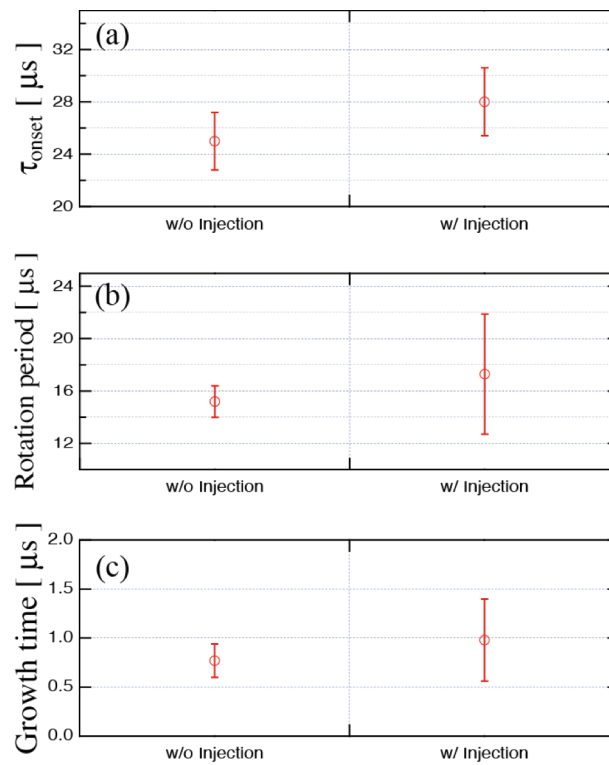


Fig.5.2. Comparison of characteristic parameters of rotational instability between injection and no-injection case.

### 5.3. Discussion

It is conjectured that the single side injection exerts two different effects, positive one and negative one, on the rotational instability. To distinguish those two effects, difference between the cases in which the single side injection improved or degraded the sustainment has been investigated. Figure 5.3 shows the time evolutions of poloidal flux and axial displacement of FRC for three injection cases (red curves). The blue curve indicate the reference case without injection. In the degraded discharge shown in (a) and (b), it was found that the FRCs tended to be moved in axial direction. The axial motion was considered to be caused by the pressure of the magnetized plasmoid injected from  $+z$ -direction. The discharge shown in (c) and (d) also shows axial bounce motion. The FRC plasma was once pushed in the negative  $z$ -direction and then restored to the original location. The poloidal flux once decreased in parallel with the FRC's axial motion, but eventually the FRC is sustained longer than the case without injection. On the other hand, prolonged decay time and increased poloidal flux was observed in stable case in which axial displacement of FRC was negligible in equilibrium phase ( $10 - 40 \mu\text{s}$ ) as shown in fig.5.3.(e) and (f). The reason why the FRC was not moved in this discharge has not been clarified yet, but it is conjectured that the single side injection often causes the axial displacement which significantly degrade the FRC's sustainment.

In conclusion, the magnetized plasmoid injection could have positive impact on FRC's sustainment and suppression effect on rotational instability; however, those favorable results were often covered by the FRC's axial displacement. In order to avoid this axial motion caused by plasmoid injection and to clarify the stabilization mechanism, I suggested a new experimental concept of double side plasmoid injection.

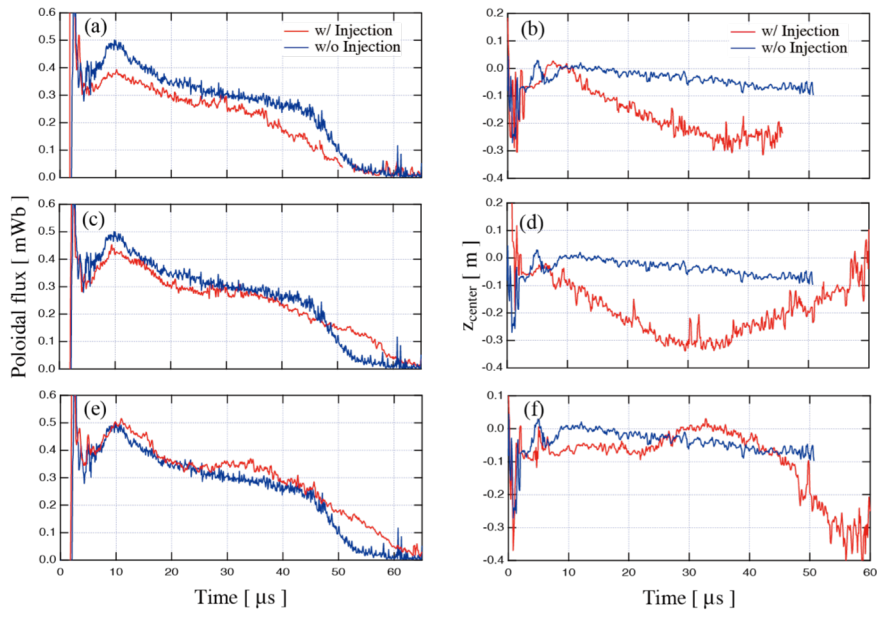


Fig.5.3. Time evolutions of poloidal flux and  $z$ -displacement of FRC's midplane.

## 6. Results from double side injection experiment

### 6.1. Conditions for plasmoid injection into FRC

Since the plasmoid injection will cause variety of changes in the FRC plasma, for example, injection of poloidal and/or toroidal magnetic fluxes, injection of particles, and so on. These changes should be investigated separately for appropriate performance evaluation of the plasmoid injection method. In this experiment, magnetic conditions for plasmoid injection could be adjusted by changing the polarity of MCPG electrode and the direction of bias magnetic field of MCPG. The polarity of the MCPG electrode could change the direction of toroidal flux of plasmoid and the direction of bias field could change the direction of poloidal flux of plasmoid. These conditions are summarized infig.6.1 (a). Based on the magnetic flux polarities of injected plasmoid, I categorized the double side injection conditions into two different cases named PI and PTI.

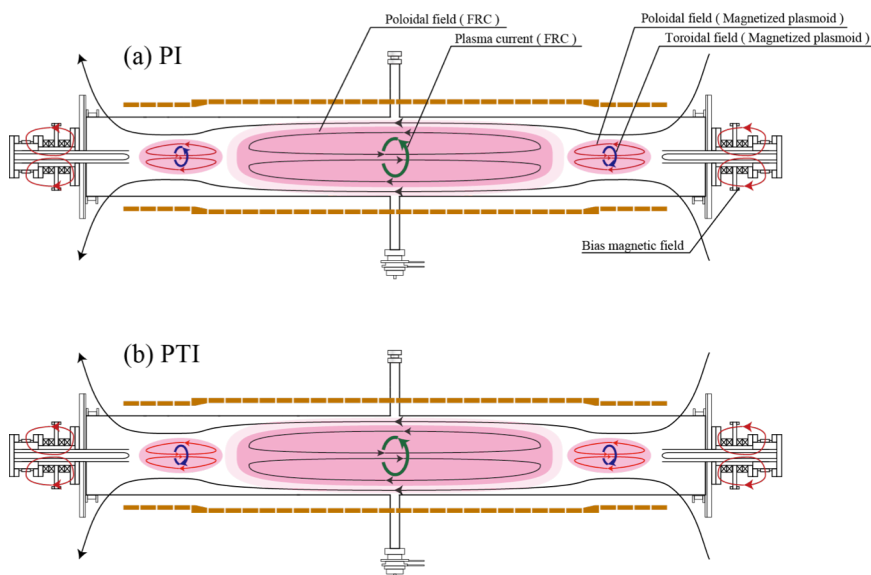


Fig.6.1. Experimental conditions of (a) PI (Poloidal flux is remained and toroidal flux is canceled after injection) and (b) PTI (Poloidal flux and toroidal flux are remained after injection)

In the condition of PI (Poloidal flux Injection), two magnetized plasmoids have toroidal fluxes in opposite direction and poloidal fluxes in same direction as shown in fig.6.1. The poloidal fluxes of the two plasmoids are also in same direction with that of the FRC, supplying net poloidal flux into the FRC. On the other hand, the toroidal fluxes in two plasmoids will cancel each other.

In the condition of PTI (Poloidal flux and Toroidal flux Injection), two magnetized plasmoids have both poloidal and toroidal fluxes in the same direction as shown in fig.6.1 (b). Thus in this condition both toroidal and poloidal fluxes will be injected into the FRC plasma.

## 6.2. Typical discharge sequence with NUCTE-III and MCPG

Since the discharge duration of FRC is much shorter than 1 ms, quick formation and injection of magnetized plasmoid is required. Figure 6.2 shows the time sequence of typical FRC discharge in NUCTE-III and waveforms of MCPG discharge. At first, discharge gas of deuterium is puffed into the FRC discharge tube (fig.6.2 (a)). Typical filling-pressure is 1.5 mTorr measured after discharge. Then deuterium gas for MCPG discharge is puffed into MCPG. After discharge gas is filled in the discharge tube, a bias field of NUCTE-III is applied by the theta-pinch coil (fig.6.2 (b)) and a bias field of MCPG is applied by the bias coil (fig.6.2 (c)). After the ramp up of the bias field, pre-ionized plasma is formed by theta pre-ionization method. Then main compression field is applied to form a FRC plasma. In this research, magnetized plasmoid is injected during the quasi-steady phase of the FRC. MCPG discharge is initiated at about the same time with the FRC's main compression field. Figure 6.2(d) shows the typical discharge waveform of MCPG currents which also produce the plasmoid's toroidal flux. Half cycle of the current is 70  $\mu$ s. Since the sign of magnetic helicity is determined by the direction of toroidal field of a magnetized plasmoid, sign of magnetic helicity changes after half cycle.

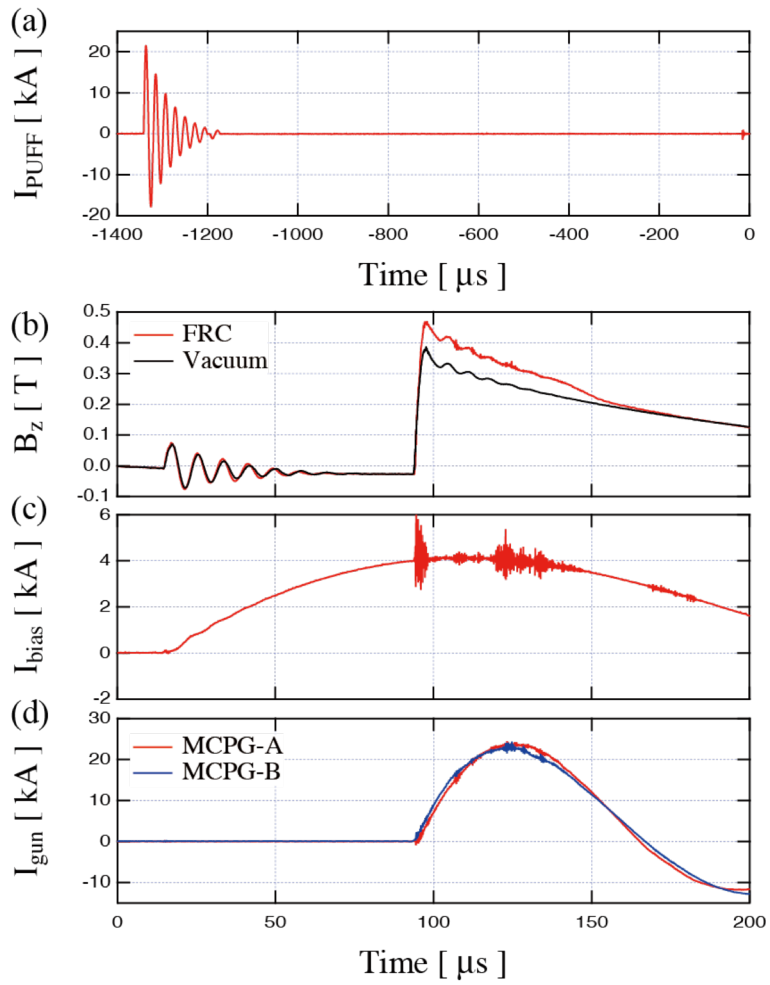


Fig.6.2. Typical discharge waveform of discharge sequence of an operation

### 6.3. Impact of neutral gas from MCPG

Before the plasmoid injection experiments were carried out, the impact of gas puff for MCPG was evaluated. Here, only the gas was puffed without MCPG discharge to see whether it might affect the behavior of the FRC plasma.

Figure 6.3 shows time evolutions of FRC's line integrated density, total temperature, ion temperature and separatrix radius measured on the mid plane ( $z=0$ ) for the cases with and without the gas puff. It was concerned that a gas from the MCPG flows into FRC, increasing the electron density and decreasing the plasma temperature. Although the electron density of both cases showed difference in a radial

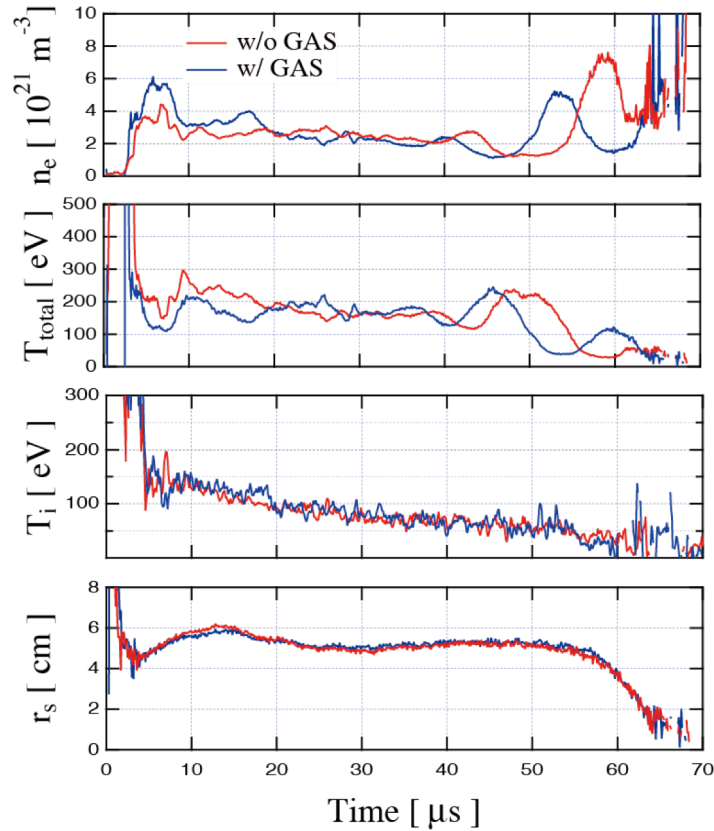


Fig.6.3. Time evolutions of typical FRC parameters with gas of MCPG and without gas of MCPG

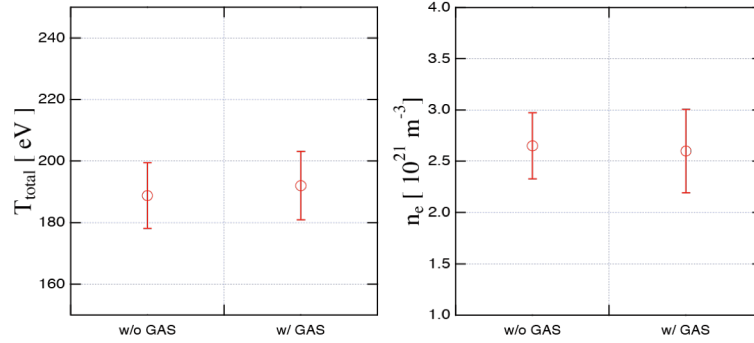


Fig.6.4. Averaged value of total temperature and electron density in both cases

and axial compression phase (0~15  $\mu\text{s}$ ), the electron density in equilibrium phase was nearly same in both cases. Typical value of electron density was  $2\text{-}3 \times 10^{21} \text{ m}^{-3}$  in these conditions. The time evolutions of total and ion temperatures agreed well in both cases with and without gas puffing. The time evolution of separatrix radius in both cases also showed no significant difference. Figure 6.4 shows the time-averaged total temperature and electron density with standard deviation in both cases. It is clear that the gas from the MCPG do not affect the FRC plasma.

#### 6.4. Experimental results of double side injection

##### 6.4.1. Difference of time evolution of separatrix radius and poloidal flux

By using a magnetized plasmoid injection, it is concerned that plasma temperature is decreased because of injected impurity originated from an electrode of MCPG. Figure 6.5 shows a distribution of line spectrum measured at center of mid-plane. Red line indicates the injection case and blue line indicates a no-injection case. Observed spectrum line had no difference obviously. Additionally, decreasing of plasma temperature also has not been observed in each condition as shown in fig.6.6. The plasma temperature is compared in equilibrium state at the time of 20  $\mu\text{s}$  after main compression. From these results, an impurity from the MCPG is negligibly small and

does not decrease the plasma temperature.

Figure 6.7 shows a time evolutions of each conditions. Thick lines indicate the separatrix radii averaged for multi-discharges and highlighted area indicates the standard deviation. Increased life-time of 5–10  $\mu\text{s}$  has been observed in both cases. In addition, a separatrix radius is sustained until 40  $\mu\text{s}$ .

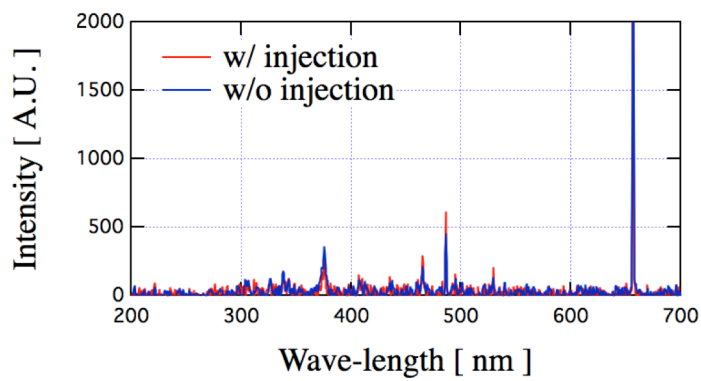


Fig.6.5. Observed line spectrum

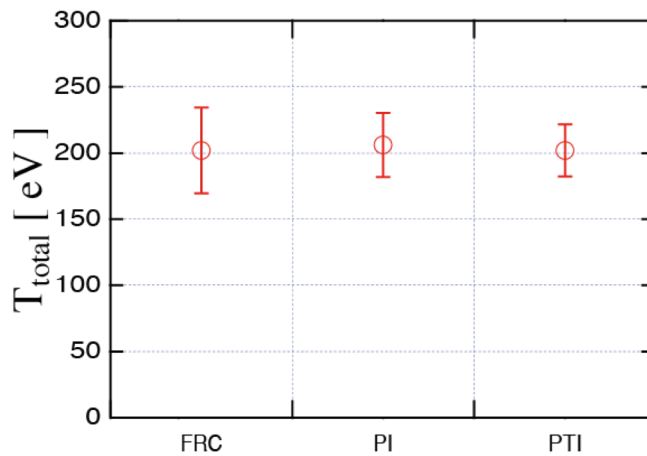


Fig.6.6 Total temperature of each condition

Time evolutions of poloidal flux is shown in fig.6.8. In this figure, a line indicates

an averaged poloidal flux and highlighted region indicates a range of the deviation as well as fig.6.7. Better sustainment of poloidal flux has been observed after injection in both injection cases. It should be noted that the poloidal flux was even increased by the plasmoid injection. The increment of the poloidal flux was observed to be about 50 – 150  $\mu\text{Wb}$ . Since one injected magnetized plasmoid has poloidal flux up to 30  $\mu\text{Wb}$ , the increment is about 0.8-2.5 times of total injected poloidal flux.

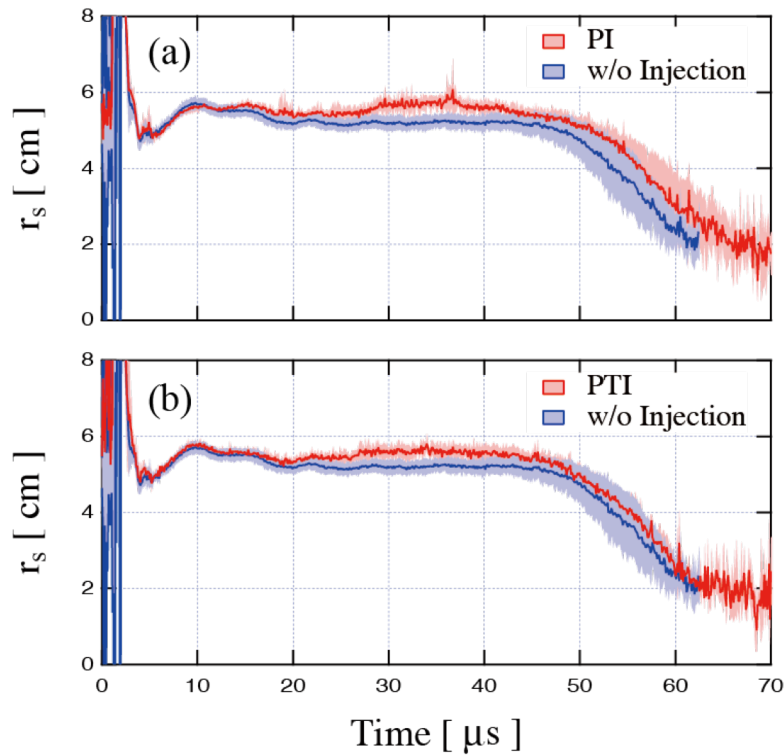


Fig.6.7. Time evolution of separatrix radius of each condition

#### 6.4.2. Stabilization effect on rotational instability

FRC generated by FRTP method is suffered from a distractive instability called rotational instability. This instability accompanies with elliptical deformation of toroidal cross section due to a strong centrifugal force. The stabilization effect on the rotational instability could be evaluated by an onset time, a rotation period and a growth time of the rotational instability. Onset time is defined as the timing of the observed elliptical deformation, growth time is defined for the elliptical deformation of plasma cross section.

Figure 6.9 shows (a) an onset time, (b) a rotation period and (c) a growth time of each condition. The plasmoid injection provides delay of onset time. The onset time of each condition is  $25\mu\text{s}$  for FRC without injection,  $35\mu\text{s}$  for PI and  $32\mu\text{s}$  for PTI. The

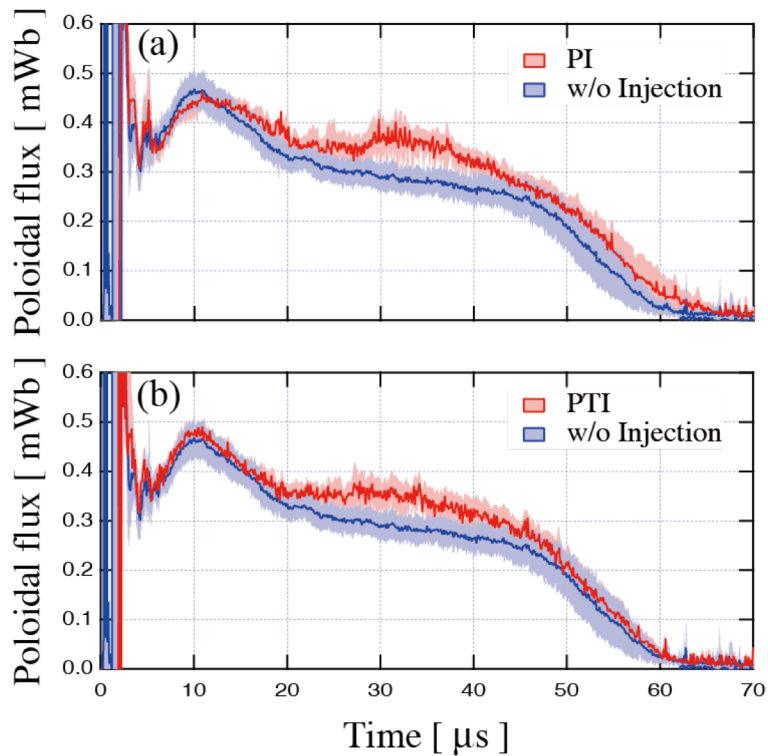


Fig.6.8 Time evolution of poloidal flux of each condition

PI case is most effective to prolong the onset timing. The rotation period exhibits similar trend of stabilization as shown in fig.6.9(b), while the discharge-to-discharge deviation is much larger than the onset timing. . The clearest trend was observed in the results of growth time. Growth time of the elliptical deformation is 2.5  $\mu\text{s}$  for PI case and 0.8  $\mu\text{s}$  for FRC without injection, respectively. Large improvement factors of 3.2 (PI) and 2.3 (PTI) were achieved by the plasmoid injection method.

By using a magnetized plasmoid injection, we have been observed significant suppression of the rotational instability. Among various injection cases, the PI case is most effective for stabilization.

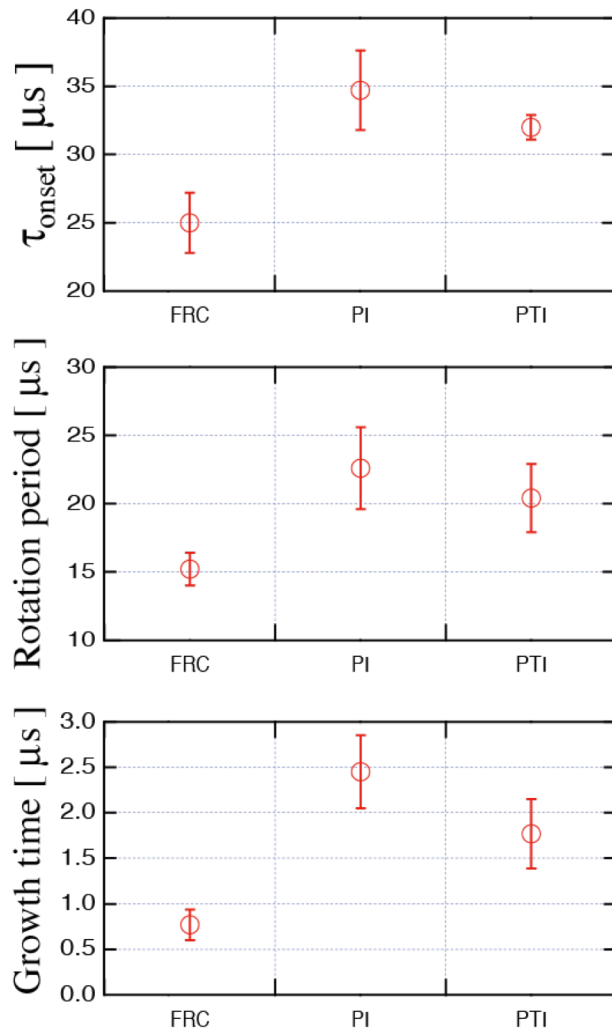


Fig.6.9. Comparison of parameters of rotational instability

## 7. Discussion

As described in chapter 6, the plasmoid injection method has a positive effect on FRC's stability. Similar stabilization of the rotational mode has also been reported in the experiments of FRC translation [1], application of a multi-pole magnetic field [2] and electrostatic biasing by using plasma gun [3]. Since the MCPG could inject variety of physical amounts such as a toroidal flux, poloidal flux, magnetic helicity, particles, thermal energy and kinetic energy, it is important to distinguish the dominant contributing factor for the stabilization. Note that the MCPG could change the electric potential profile like the biasing method. Possible candidates for the stabilization are summarized in table 7.1.

### 7.1. Evaluation of plasmoid's energy and inventory

of The contained energies of the main FRC plasma and the magnetized plasmoid are compared in table 7.2. The contained energy of magnetized plasmoid is much smaller than the energy of FRC. The largest energy content of one plasmoid was the poloidal magnetic energy of 60 J, but it corresponds only 3-4 % of the poloidal magnetic energy of the FRC. It is estimated that the injected energy of magnetized plasmoid is not sufficient to bring about a significant change on the FRC.

Since the properties of rotational instability such as rotational speed, grow speed are supposed to depend on total mass of FRC, the mass injection might suppress the instability. Figure 7.1 shows the electron density measured just after the plasmoid injection ( $t = 25 \mu\text{s}$ ), but no significant difference has been observed on each condition.

Table 7.1. Possible sources for suppression of rotational instability

	Toroidal flux	Poloidal flux	Inventory	Thermal energy	Biasing effect
PI	×	○	○	○	○
PTI	○	○	○	○	×

Table 7.2. Comparison of energies contained in FRC and magnetized plasmoid

	$E_{\text{thermal}} [ \text{J} ]$	$E_{\text{kinetic}} [ \text{J} ]$	$E_{\text{poloidal}} [ \text{J} ]$	$E_{\text{toroidal}} [ \text{J} ]$
FRC	$2.6 \times 10^3$	-	$1.8 \times 10^3$	-
Plasmoid	2.6	0.1-0.3	60	55

The total inventory of the target FRC of  $10^{19}$  [particles] is about 100 times larger than that of the injected magnetized plasmoid of  $10^{17}$  [particles]. It is conjectured that the mass injection is not the dominant factor for suppression of the rotational instability, either.

The energy injection and mass injection should be omitted from the candidates for stabilization. The remaining candidates for PI / PTI cases are shown in table 7.3. Since both the PI and the PTI cases showed mitigation of the rotational instability and resulting longer sustainment of the FRC plasma, it is considered that the poloidal flux injection is a potential candidate for the stabilization of the rotational mode in this experiment. In this section, I'll discuss about the effect of the poloidal flux injection on FRC plasma and then consider about the other candidates which will bring about the difference between the PI and PTI cases.

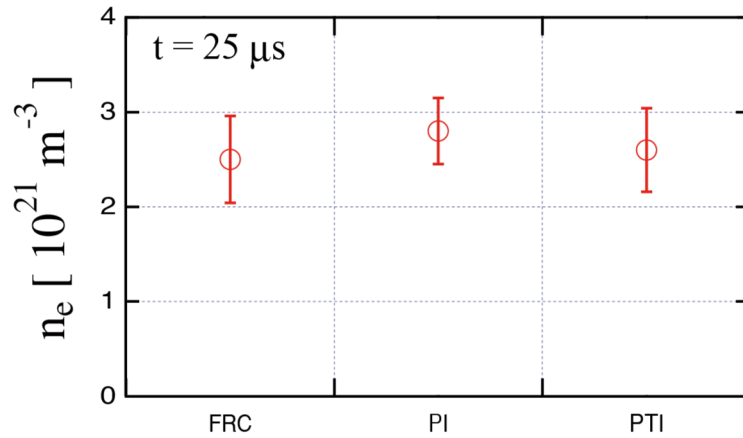


Fig.7.1 Electron density measured at the timing of after injection ( $t = 25 \mu\text{s}$ )

Table 7.3. Remaining candidates as sources of stabilization

	Toroidal flux	Poloidal flux	Biasing effect
PI	×	○	○
PTI	○	○	×

## 7.2. Comparison between Single injection and Double injection

From the discussion in the previous section, one of the potential candidates providing the mitigation effect of rotational instability is poloidal magnetic flux injection, which was commonly supplied in both PI and PTI cases. Here, I'll compare the cases of PI, PTI and single injection to evaluate the poloidal flux injection effect.

In this evaluation, the conditions of MCPG were set as; discharge current of about 25 kA, bias flux of about 1.2 mWb. Figure 7.2.(a) shows time evolutions of poloidal flux of the main FRC measured on the mid plane for each case. The markers in the graph indicate averaged poloidal flux and the error bars show standard deviation. In plasmoid injection case, poloidal flux of the main FRC was enhanced compared with non-injection case. Clear difference appeared among these cases after 15 μs. Figure 7.2.(b) shows the time evolution of poloidal flux increment of each injection case from the no-injection case. The PI case showed the largest increment in the three cases,

but the PTI case also showed larger increment than the single injection case. The increment of poloidal flux reached up to about 100  $\mu\text{Wb}$  in the PI case, 70  $\mu\text{Wb}$  in the PTI case and 50  $\mu\text{Wb}$  in the single injection case. These results suggest that the plasmoid injection could induce even larger poloidal flux than that included in the original plasmoid; about 30  $\mu\text{Wb}$  per a plasmoid. Thus, injection of magnetized plasmoid possibly worked to increase plasma current of a FRC by some mechanism. The increment of poloidal magnetic flux in PI and PTI cases appeared in the earlier phase than in the single injection case, as shown in fig.7.2.(c). This quick response in the double injection cases is possibly due to the smaller axial motion of the main FRC.

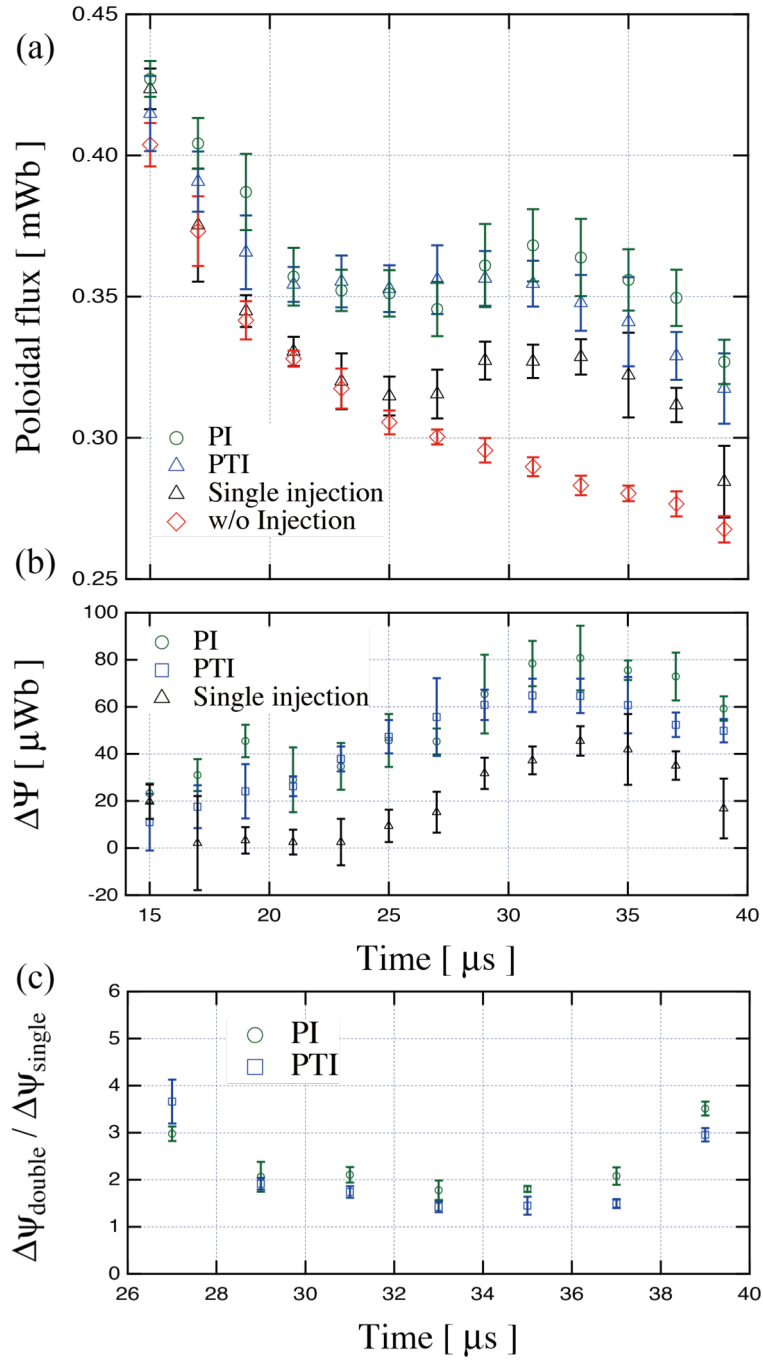


Fig.7.2. Comparison of main FRC's poloidal flux for cases with / without plasmoid injection.

(a) shows time evolutions of main FRC's poloidal flux (green circle is PI, blue square is PTI, black triangle is single injection and red rhombus is no-injection case). The increment of poloidal flux from no-injection case is shown in (b), and the ratio of double injection case and single injection case is shown in (c).

### 7.3. Poloidal flux increment dependence on gun voltage and bias field

Increment of poloidal flux was clearly observed in the PI and PTI case. Here, its dependence on the plasmoid flux is evaluated. Figure 7.3 shows a time evolution of main FRC's poloidal flux of PI and PTI cases together with no-injection case with (a) MCPG voltage of  $V_{\text{gun}} = 5 \text{ kV}$  and (b) MCPG voltage of  $V_{\text{gun}} = 6 \text{ kV}$ . In both gun voltage cases, increment of main FRC's poloidal flux was observed in injection cases (PI and PTI). The increment of poloidal flux in the PI case was slightly higher than the PTI case, and the life time of the PI case was prolonged about 5-10  $\mu\text{s}$  from the no-injection case. The lifetime extension was more remarkable when gun voltage was higher.

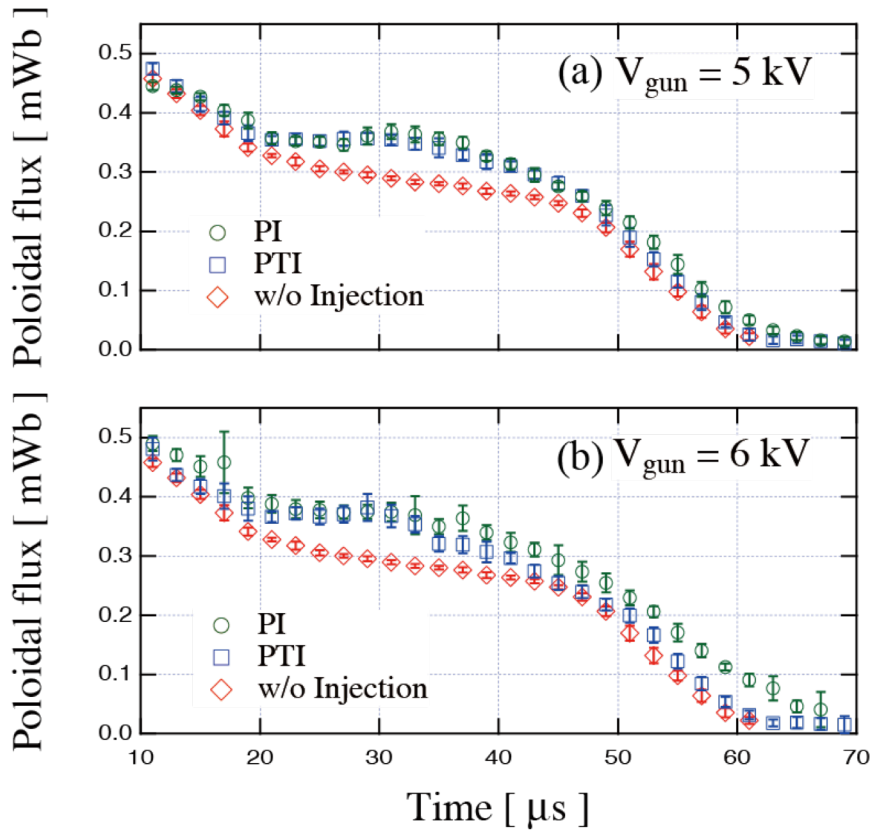


Fig.7.3. Time evolutions of main FRC's poloidal flux of (a)  $V_{\text{gun}} = 5 \text{ kV}$  and (b)  $V_{\text{gun}} = 6 \text{ kV}$ . In this graph, green circle indicates the PI case, blue square indicates the PTI case and red rhombus indicates the no-injection case.

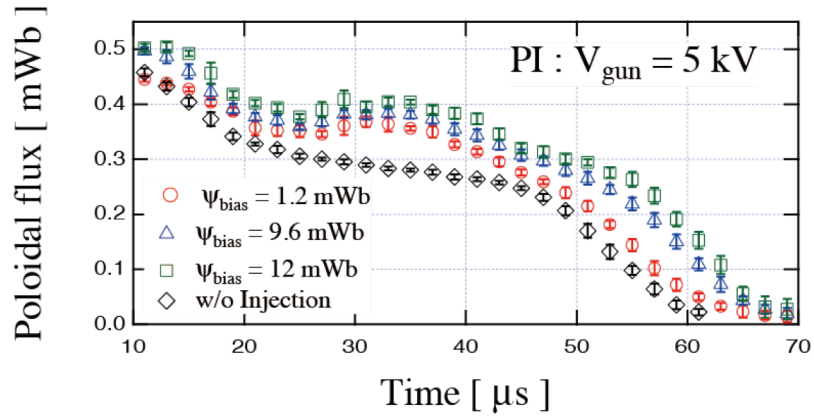


Fig.7.4. Time evolutions of the poloidal flux for various bias flux cases.

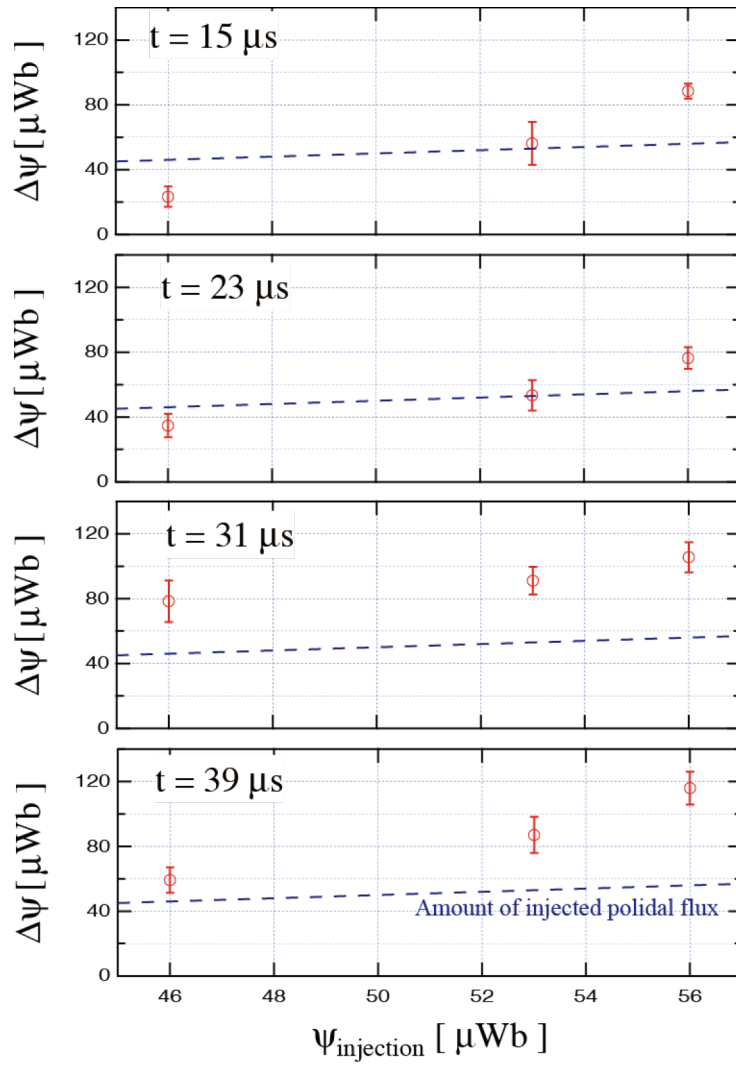


Fig.7.5. Injected poloidal flux dependence of increased poloidal flux. Blue dashed line indicates a predicted amount of injected poloidal flux.

The increment of the main FRC's poloidal flux also depends on the bias magnetic flux of the MCPGs. Figure 7.4 shows a time evolution of main FRC's poloidal flux for three different bias flux cases of  $\psi_{\text{bias}} = 1.2$  mWb (red circle), 9.6 mWb (blue triangle) and 12 mWb (Green square). Increment of main FRC's poloidal flux was observed in every case, and larger increment of poloidal flux and longer extension of FRC's lifetime was observed for larger bias flux case. Fig. 7.5 shows the dependence of the increment of the main FRC's poloidal flux on the MCPG bias flux. The poloidal flux increment gradually increases as time.

In 7.1-7.3, the response of the main FRC to the plasmoid injection was evaluated from the evolution of FRC's poloidal flux. The achieved findings are; (1) Double side plasmoid injection showed larger increment of the main FRC's poloidal flux than the twice the increment of the single injection, (2) poloidal flux only injection (PI case) is more effective for the enhancement of main FRC's poloidal flux and extension of lifetime, and (3) larger poloidal flux included in the magnetized plasmoid brings about larger increment of the main FRC's poloidal flux.

#### 7.4. Suppression effect on FRC's toroidal rotation

A FRC has a strong spontaneous toroidal flow inside the closed field region. The spin-up mechanism has not yet well understood yet, but the rotation frequency gives the threshold for the FRC's elliptic deformation. The normalized rotation frequency  $\alpha$  is defined as  $\alpha \equiv \Omega/\Omega_{\text{D.I.}}$  [4], where  $\Omega$  is a rotation frequency and  $\Omega_{\text{D.I.}}$  is the ion diamagnetic drift frequency. It is predicted that the rotational instability of  $n = 2$  mode grows when the ion rotation exceeds the diamagnetic drift as  $\alpha > 1.2-1.4$ , and the mode grows faster for  $\alpha > 1.6$  [5]. Thus, in order to evaluate the plasmoid injection effect on the rotational mode, it is required to observe the FRC's rotation velocity. Here, the results from impurity ion Doppler spectroscopy will be presented.

Flow velocity measured at  $r = 3\text{cm}$  on the mid-plane was compared for the PI, PTI, no-injection cases. Figure 7.6 shows a time evolution of toroidal flow velocity with standard deviation shown by error bars. In fig 7.6, red circle indicates the flow in the PI case, blue circle indicates that in the PTI case and green circle indicates that in the no-injection case. In each case, toroidal flow velocity gradually increases with time in 10-25  $\mu\text{s}$ , but the injection cases (PI and PTI) showed slower flow velocity than the no-injection case. About 30 % of rotation slow-down has been observed in injection

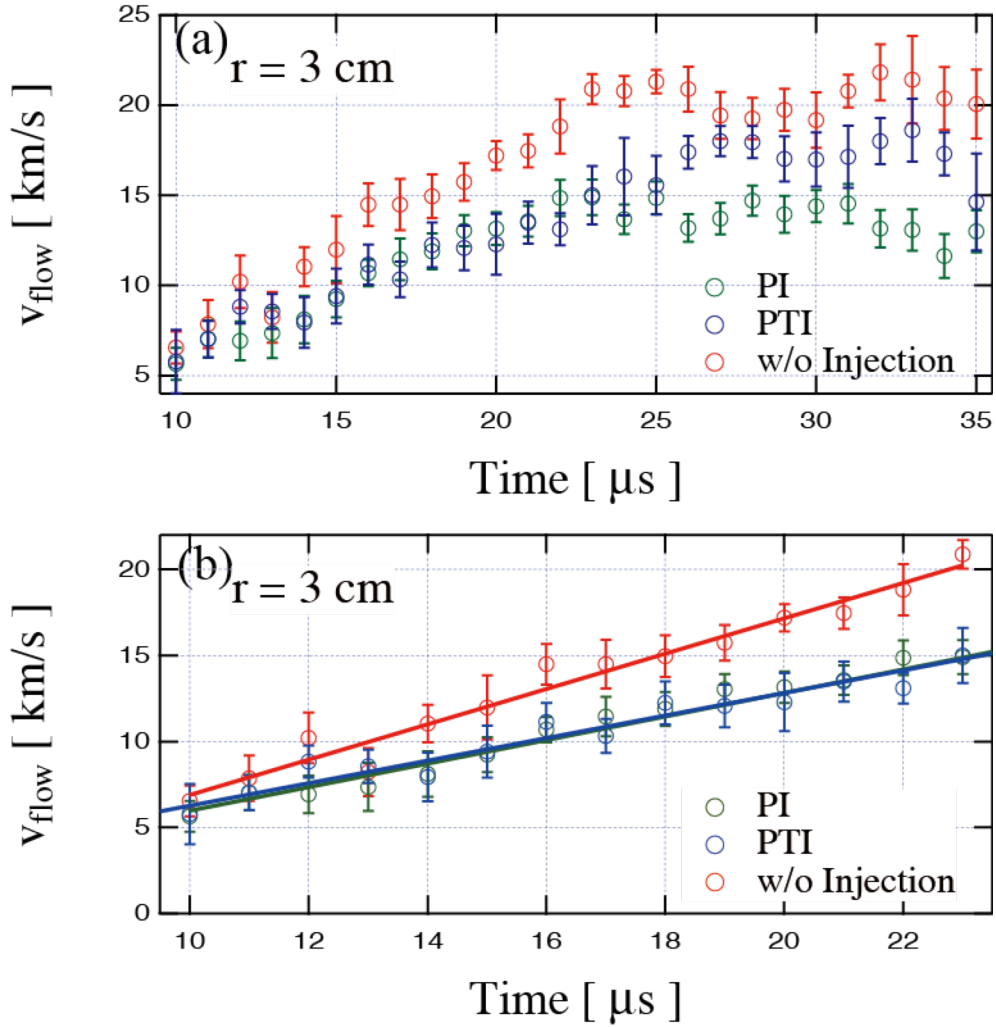


Fig.7.6. Time evolution of flow velocity measured at  $r=3$  cm. (a) shows a flow velocity of each conditions. The gradients of flow is shown in (b).

cases. After  $25 \mu\text{s}$ , the flow velocity of the PI case was maintained about 13-15 km/s, which was even slower than the PTI case. The acceleration of the toroidal flow was also suppressed in the PI and PTI cases for 10-25  $\mu\text{s}$  as shown in fig.7.6 (b). Since the FRC showed linearly increasing toroidal flow velocity in each case in this phase, the FRC was supposed to be subjected to almost constant azimuthal torque. The acceleration of PI and PTI were  $6.8 \times 10^8 \text{ m/s}^2$  and  $6.5 \times 10^8 \text{ m/s}^2$ , respectively. On the other hand, higher acceleration of about  $10 \times 10^8 \text{ m/s}^2$  was observed in no-injection case. It is concluded that the plasmoid injection could reduce the acceleration to 65-70 % of that of no-injection case.

The rotational instability of  $n = 2$  mode grows faster when the normalized rotation frequency  $\alpha$  is greater than 1.6 as mentioned above. Assuming the FRC has an axisymmetric field and is expressed as a rigid rotor model, diamagnetic drift frequency is expressed as

$$(\Omega_{*})_{RR} \approx \left(\frac{3}{2}\right)^{1/2} \left(\frac{r_s}{r_c}\right) \Omega_0 \quad (1)$$

$$\Omega_0 \equiv -\frac{8k_B T_{i,m}}{eB_e r_s^2} [5]$$

, where  $r_c$  is a coil radius,  $r_s$  is a separatrix radius and  $T_{i,m}$  is a maximum temperature. The diamagnetic drift frequency is obtained by substitution of the experimentally measured values. In this experiment,  $(\Omega_{*})_{RR}$  is 480-490 krad/s for  $\alpha = 1.2$  and  $(\Omega_{*})_{RR}$  is 640-660 krad/s for  $\alpha = 1.6$ . The rotation frequency for the injection and no-injection cases are shown in fig.7.7. Figure 7.7 (a) shows the time evolution of normalized ion rotation frequency of the FRC without injection case, (b) of the FRC with PI and (c) with PTI. In fig.7.7., aqua color highlighted region corresponds to  $\alpha = 1.2$  and orange highlighted region corresponds to  $\alpha = 1.6$ . The normalized rotation frequency of no-injection case increased monotonically and reached the  $\alpha = 1.2$  threshold at 21-22  $\mu$ s, then reached  $\alpha = 1.6$  threshold at 33  $\mu$ s. On the other hand, the normalized rotation frequency of the PI and PTI cases increased until 23-25  $\mu$ s and then stopped increasing after 25  $\mu$ s. Both PI and PTI cases got to the  $\alpha = 1.2$  threshold at 24  $\mu$ s but never reached the  $\alpha = 1.6$  threshold. This reduced rotation frequency in the injection cases might be responsible for the delayed onset timing of the elliptic deformation and extended rotation period.

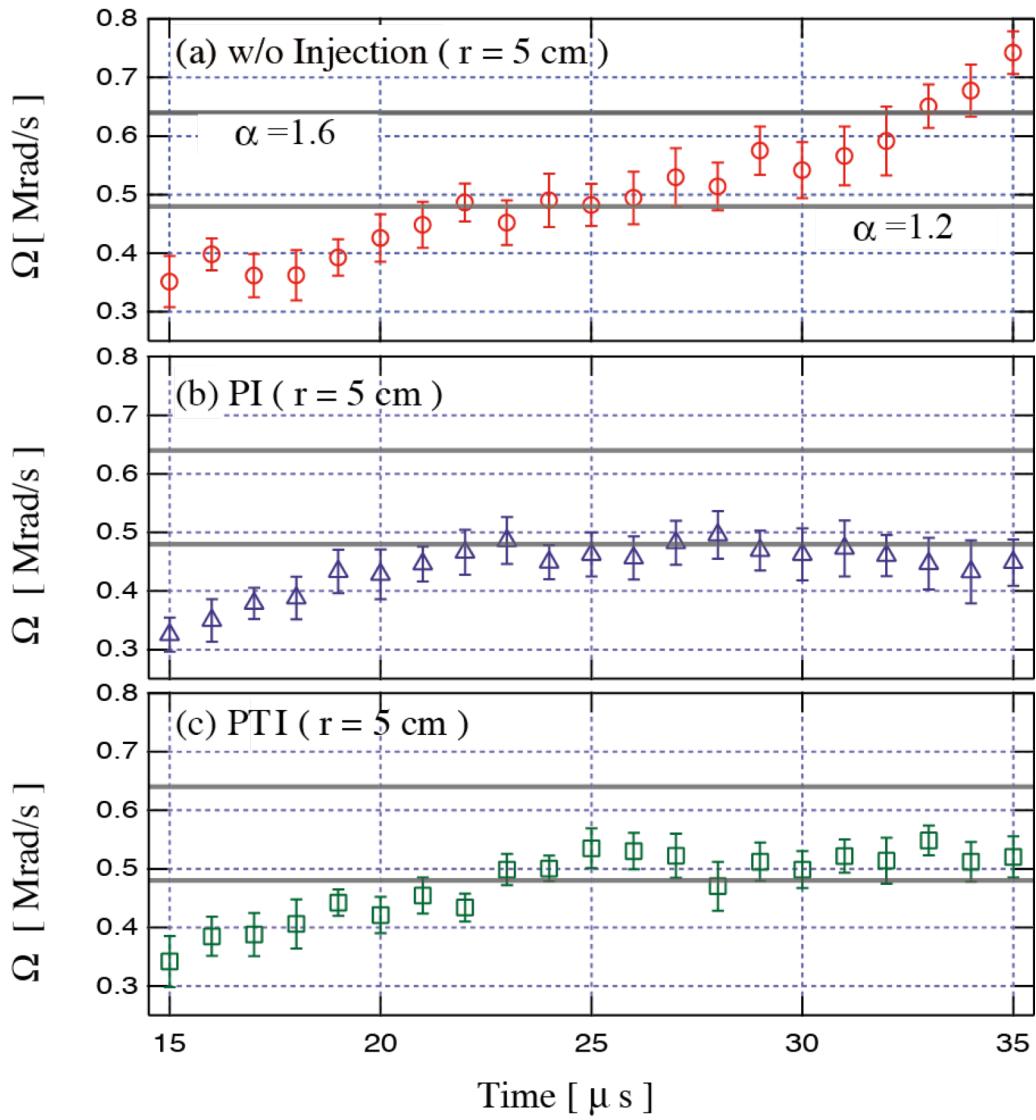


Fig.7.7. Time evolutions of rotation frequency of each case : (a) no-injection case, (b) PI case and (c) PTI case. Blue highlighted region is a threshold in which  $n=2$  rotational mode starts to grow ( $\alpha=1.2$ ) and orange highlighted region is also threshold in which the rotational mode grow faster ( $\alpha=1.6$ ).

### 7.5. Flux decay theory [6] and stabilization effect by plasmoid injection

As described in section 7.3, increment of the main FRC's poloidal flux was observed by magnetized plasmoid injection. Also in section 7.4, reduced rotation frequency was addressed. In this section, a relation between the poloidal flux increment and rotation frequency reduction will be discussed based on the flux decay theory [6].

The flux decay theory suggests one of possible mechanisms for the FRC's spontaneous rotation proposed by T. Takahashi. Given that the FRC has an axisymmetric confinement field, angular momentum is conserved for all particles in FRC. The angular momentum is expressed as the following eq (2) and if the angular momentum is conserved, each ion should follow eq (3).

$$P_{\theta} = mrv_{\theta} + q \frac{\psi}{2\pi} \quad (2)$$

$$m \Delta (rv_{\theta}) = -q \Delta \left( \frac{\psi}{2\pi} \right) \quad (3)$$

, where  $P_{\theta}$  is an angular momentum and  $\Psi$  is a poloidal flux function. From eq.(3),  $rv_{\theta}$  should increase when poloidal flux decreases in time. Moreover if the radius of the ion's orbit also decreases or sustained, the toroidal flow velocity must increase in time. Then eq.(3) can be rearranged as

$$\frac{\Delta (rv_{\theta})/\Delta t}{\Delta\psi/\Delta t} = -\frac{q}{2\pi m} = \text{const.} \quad (4)$$

Therefore, the ratio of  $rv_{\theta}$  and  $\Psi$  will indicate whether the experimentally observed spin-up is amenable to the flux decay theory. Figure 7.8 shows a typical time evolution of poloidal flux and  $rv_{\theta}$  in the no-injection case. These data were achieved in a single discharge. Here, change rates of poloidal flux and  $rv_{\theta}$  were calculated from a gradient of the curves of poloidal flux and  $rv_{\theta}$  in two different periods of 10-20  $\mu\text{s}$  and 20-35  $\mu\text{s}$  as shown in fig.7.8. The gradients values for this discharge are shown in table 7.4. The relation between  $\Delta(rv_{\theta})$  and  $\Delta\Psi$  obtained from many discharges is shown in fig.7.9. The value of  $rv_{\theta}$  increased when the poloidal flux decreased in time, suggesting that  $\Delta(rv_{\theta})$  and  $\Delta\Psi$  have a linear relationship as predicted from the flux decay theory. Though the experimentally observed gradient of  $\Delta(rv_{\theta})/\Delta t \sim 4.9 \text{ m}^2/(\mu\text{Wb s})$  was much smaller than the predicted value of  $7.5 \text{ m}^2/(\mu\text{Wb s})$ , they also shows good correlation in their time evolutions.

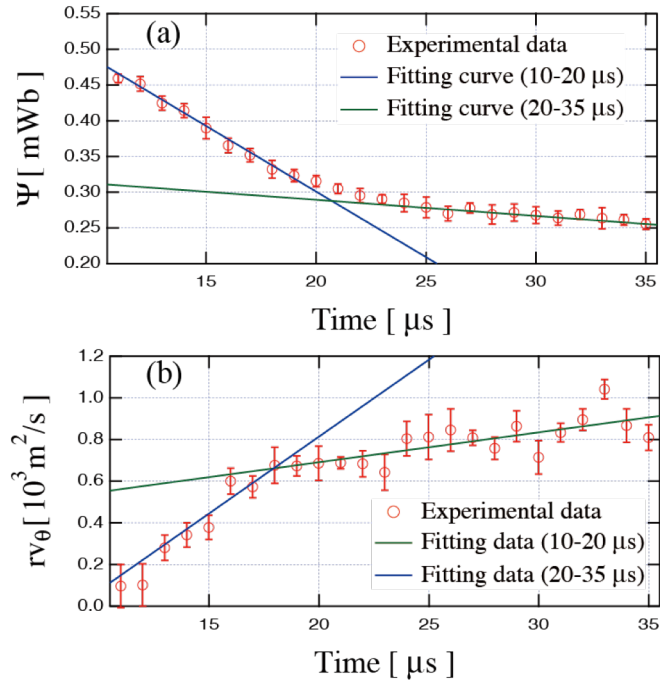


Fig.7.8. Time evolutions of (a) poloidal flux and (b)  $rv_\theta$ . The blue line indicates a fitting curve calculated in 10-20  $\mu\text{s}$  and Green line indicates a fitting curve calculated in 20-35  $\mu\text{s}$ .

Table 7.4. Achieved gradient values of  $\Delta(rv_\theta)/\Delta t$  and  $\Delta\Psi/\Delta t$

Calculated time	$\Delta\Psi/\Delta t$	$\Delta(rv_\theta)/\Delta t$
10-20 $\mu\text{s}$	-18 $\mu\text{Wb}/\mu\text{s}$	73 $\text{m}^2/\mu\text{s}$
20-35 $\mu\text{s}$	-2 $\mu\text{Wb}/\mu\text{s}$	14 $\text{m}^2/\mu\text{s}$

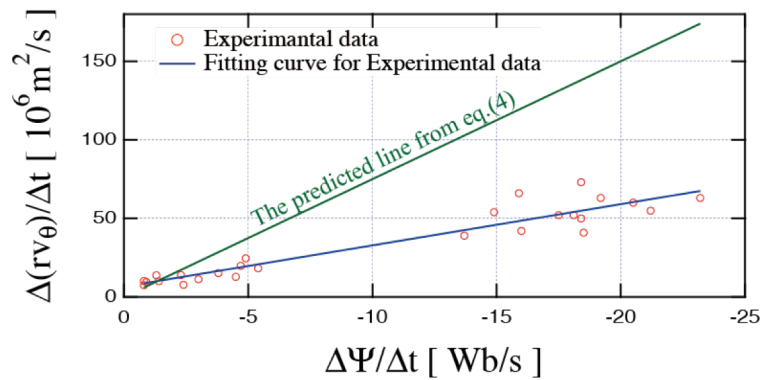


Fig.7.9. The relation between  $\Delta(rv_\theta)$  and  $\Delta\Psi$  calculated from the data of toroidal flow

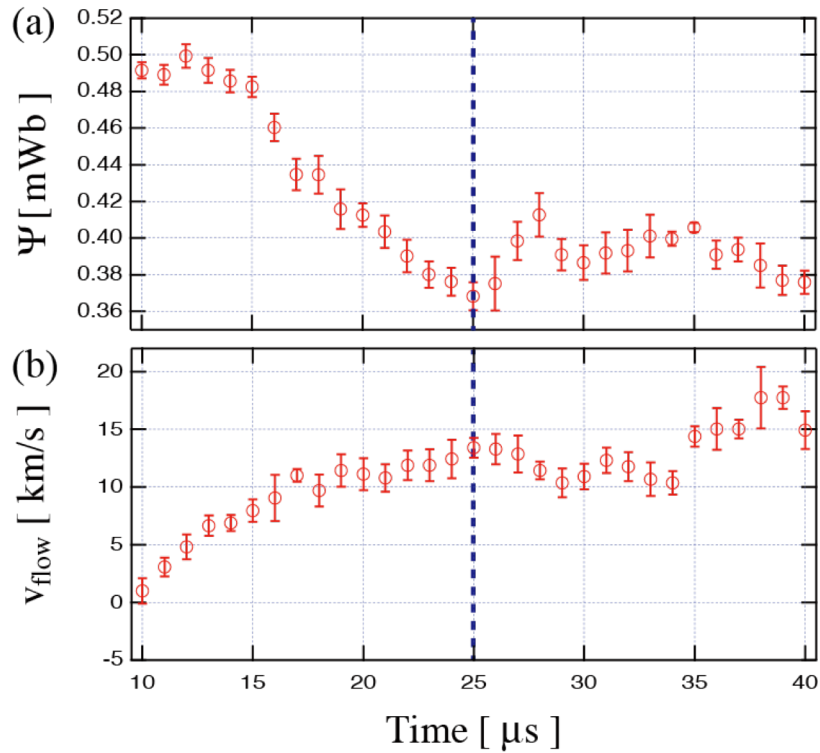


Fig.7.10. The time evolutions of (a) main FRC's poloidal flux and (b) toroidal flow in the case of PI injection which brought about remarkable increment of poloidal flux together with rotation speed reduction.

Figure 7.10 shows a typical time evolutions of poloidal flux and toroidal flow speed in FRC with PI injection case. In this discharge, remarkable increment of poloidal flux was observed together with a reduction of the rotation speed. The main FRC's poloidal flux started to increase at the timing indicated by blue dashed line, and toroidal flow speed also started to decrease at almost same timing. By the plasmoid injection, the main FRC's poloidal flux increased 44  $\mu\text{Wb}$  from 25  $\mu\text{s}$  to 28  $\mu\text{s}$ . At the same timing, the flow speed reduced about 3 km/s, which is close to the  $\Delta v_{\theta}$  of 2.7 km/s expected from the experimental value from Fig. 7.9. This quick response of the rotation velocity on the poloidal flux change suggests the existence of some direct conversion mechanism between poloidal flux and rotation, such as conservation of canonical angular momentum.

## 7.6. Summary of the discussion

In this section, detailed analysis on the plasmoid injection has been presented. The results are summarized as follows:

- (1) Decreasing of elliptic deformation and the period of the FRC rotation have been observed in plasmoid injection (PI and PTI).
- (2) A poloidal flux was increased and decay of poloidal flux was decreased.
- (3) Configuration lifetime was prolonged.
- (4) The effects of (1) and (2) were enhanced to increase an injected poloidal flux of plasmoid.
- (5) Spin up rate was dropped down.
- (6) Angular frequency was decreased and the frequency was sustained after equilibrium phase.
- (7) poloidal flux of FRC has a positive correlation with product of separatrix radius and toroidal flow.

From these results, the plasmoid injection (PI and PTI) mitigated the rotational instability. Growth of the rotational instability is related to a rotation frequency of the FRC. In the injection case (PI and PTI), the rotation frequency was sustained at 1.2 times of ion diamagnetic frequency that is the threshold of onset of rotational instability although the angular frequency of no-injection case was monotonically increased in time. Therefore a control of the rotation frequency of the FRC by magnetized plasmoid injection is effective for the suppressing of the rotational instability.

In addition, increasing of poloidal flux was observed in injection case. This may be that plasma current was driven by the injected magnetized plasmoid. Furthermore the good correlation between a flux change and canonical momentum change. Therefore amplified poloidal flux is one of possibly mechanism of the sustainment of angular frequency of injection case.

[1]D.J. Rej, et al, Phys. Fluids **29**, 8 (1986)

[2]R.D.Milroy and L.C.Steinhauer, Phys.plasma. **15**, 022508 (2008)

[3]M. Tuszewski,, et al, PRL **108**, 255008 (2012)

[4]M. Tuszewski, Nuclear fusion **28**, 11 (1988)

[5]L.C. Steinhauer, POP **15**, 012505 (2008)

## 8. Conclusion

### 8.1. Summary of the chapters of this thesis

In the chapter 1, background and motivation of this research were presented. Although FRC has many attracting features, it often suffers from destructive rotational instability with toroidal mode number of  $n = 2$ . One of the most important and interesting issues of FRC research is to clarify and control its spontaneous rotation. In this research, magnetized plasmoid injection has been employed as a novel active control method of FRC's rotational instability by using MCPGs.

In the chapter 2, the theories considered as the rotation mechanisms were described. In general, FRC plasma starts to rotate with diamagnetic direction immediately FRC was formed. Then the rotating speed is increased in times, and rotational instability has started and grown when the rotation speed reached the threshold value. Therefore the significance of understanding for rotational instability was described, and possible theories of rotation mechanism were shown in this chapter.

In the chapter 3, experimental setup of the theta-pinch FRC device NUCTE-III was addressed together with the brief description of FRC formation method and the derivation principle for FRC parameters from common diagnostics. Detail of the optical diagnostics for the measurements of FRC's elliptic deformation and rotation velocity were described.

In the chapter 4, newly developed MCPG system was described. Overview of the power supply and derivation of plasma gun parameters regarding helicity injection were shown. Performance of the MCPG was evaluated in a test chamber with internal magnetic probe, time-of-flight emission measurement and spectroscopy. It was confirmed that the developed system could produce magnetized plasmoid with necessary magnetic flux, velocity, and reduced impurity.

In the chapter 5, the experimental results from single side plasmoid injection were described. In this experiment, a magnetized plasmoid was axially injected from one side to FRC to supply both the poloidal and toroidal fluxes in a short period. The effect of plasmoid injection was evaluated by the FRC parameters such as trapped flux and the elliptic deformation parameters such as onset time, rotation period and growth time. This single side injection experiment resulted in bad reproducibility. In some discharges improved lifetime was observed due to the suppression of the rotational instability, but in some discharges the lifetime was degraded. Detailed measurement showed that the

degradation was caused by the axial shift motion of the FRC plasma induced by the injected plasmoid from one side, however, plasmoid injection provided suppression of the rotational mode in some discharges in which the axial shift was negligible. This results led me to utilize double side injection technique to cancel the axial motion of the FRC.

In the chapter 6, the experimental results from double side plasmoid injection were described. Different from the single side injection, the double side injection has two injection modes; the one is the poloidal flux injection (PI) mode in which the toroidal fluxes included in the two plasmoids are opposite and will cancel out after injection. The other is the poloidal and toroidal fluxes injection (PTI) mode in which the two plasmoids have the toroidal fluxes in the same direction. Both PI and PTI cases showed suppression effect on the elliptic deformation of the rotational instability and the FRC's lifetime was extended. The PI case generally exhibited more effective suppression of the rotational mode than the PTI case. This result suggests that the injection of the toroidal flux, which was predicted to improve the FRC's stability, is not essential to stabilize the rotational mode. Important achievement was that the double side injection provided the increase of the FRC's poloidal flux during the monotonically decaying phase.

In the Chapter 7, the mechanism of rotational stability improvement by the plasmoid injection was discussed. Comparative verification of toroidal flow velocity of the FRC with and without plasmoid injection was carried out. In both PI and PTI cases, the acceleration of the FRC rotation frequency was reduced in comparison with no-injection case. It was observed that the rotation of the FRC with plasmoid injection saturated when its angular frequency reached about 1.2 times of the ion's diamagnetic drift frequency, which is the threshold for destabilization of the rotational mode, while the angular frequency of the FRC without plasmoid injection quickly exceeded 1.6 times of the ion's diamagnetic drift frequency. The slower rotation of the FRC with plasmoid injection prevented the FRC from being destabilized against the rotational mode. Consequently, the plasmoid injection directly worked to reduce the acceleration of the FRC's spontaneous spin-up, leading to mitigation of the  $n=2$  elliptic deformation and extended lifetime. The rotation in the PI case was retained in slightly lower frequency than that in the PTI case. This observation was consistent with the results that the PI case showed better suppression effect on the rotational instability as shown in the

Chapter 6. Based on these results, the mechanism of the FRC's spontaneous rotation was investigated. Among various candidates of the spin-up mechanism, the flux decay is the most suitable to interpret the experimental results. Linear correlation between the change of the poloidal flux and the change of the canonical angular momentum was confirmed. Although the proportionality coefficient did not exactly agree with the predicted value, it is concluded that the flux decay is a plausible cause of the FRC's spin-up.

## 8.2. Conclusions

The goal of this research is to establish an active stabilize method of the FRC's rotational instability by using the magnetized plasmoid injection technique. The experimental studies were carried out by using newly developed MCPGs on NUCTE-III device. Remarkable results are:

- (1) The plasmoid injection (PI and PTI) mitigates the rotational instability. Contrary to the expectation, the PI case was more effective than the PTI case.
- (2) The plasmoid injection could provide amplification of the FRC's poloidal flux.
- (3) The spontaneous spin-up was suppressed by the plasmoid injection.
- (4) Good correlation was observed between the flux change and the canonical angular momentum change.

These results indicate that the plasmoid injection works directly to suppress the FRC's spontaneous spin-up, and the reduced rotation frequency leads to mitigate the rotational instability with  $n = 2$  elliptic deformation. The proposed method has decisive advantages in comparison with existing stabilizing techniques such as application of the multi-pole magnetic field and toroidal flux induction by translation. The multi-pole field has a critical flaw of confinement degradation, however, it has been confirmed that the plasmoid injection technique could provide both mitigation of the rotational mode and the flux increment without any destructive instabilities. Remarkable characteristic of the proposed method is that it directly reduces the FRC's spin-up, providing fundamental stabilization effect for the rotational mode. The plasmoid injection method also has a potential for repetitive or continuous operation. This feature could bring more advantages for future longer-pulse experiments. Furthermore, the plasmoid injection is a unique technique to increase the magnetic flux of the theta-pinch produced FRC plasma. It may be utilized as a current drive method to sustain the FRC plasma.

These experimental results also shed light to the mechanism of the FRC's spontaneous spin-up. Not only in the monotonically decaying phase, but also in the flux increasing phase by the plasmoid injection, the linear relationship between the flux change and the angular momentum change showed good qualitative agreement with that expected from the hypothesis which insists that the FRC's spin-up is driven on the basis of the canonical angular momentum conservation.

Finally, I will show some issues to be studied in the future:

- (1) Flux (or helicity) transport, flux conversion and current drive mechanisms.
- (2) Achievement of complete stabilization of the rotational mode.
- (3) Quantitative assessment of the FRC's spin-up mechanism.

## Acknowledgement

This research as the doctoral thesis of graduate school of frontier science in the university of Tokyo was carried out at the Nihon university. At the end of my doctoral study, I would like to express my deepest gratitude to Prof. Michiaki Inomoto whose enormous support and insightful comments were invaluable during the course of my study.

Also, I would like to express my deepest appreciation to Prof. Tomohiko Asai belonging to Nihon University. His enormous tutelage and beneficial comments have been invaluable since I was bachelor student in Nihon university.

I would like to show my greatest appreciation to Prof. Tsutomu Takahashi belonging to Nihon University. His experimental supports and encouraging comments were favorable during my experimental study.

I would like to offer my special thanks to Prof. Yoichi Hirano whose technical comments for my research and enormous tutelages for electrical circuit and magnetic hydro dynamics theory were very insightful.

I would like to express my gratitude to Prof. Toshiki Takahashi. His advices and comments about the spin-up theory with flux decay of FRC were very instructive.

In the CT-RFP workshop held in NIFS (National Institute for Fusion Science), I was extended beneficial comments and advices for implementation of my research. I would like to express my greatest thanks to academics of fusion plasma physics such as Prof. Sadao Masamune belonging to Kyoto Institute of Technology and Prof. Masayoshi Nagata belonging to University of Hyogo.

I would like to thank Prof. Yuichi Takase belonging to the University of Tokyo, Prof. Akira Ejiri belonging to the University of Tokyo and Prof. Haruhisa Koguchi belonging to AIST (National Institute of Advanced Industrial Science and Technology) whose comments for physical construal and advices for development of my doctoral thesis were very beneficial.

I would like to thank the master's course students of the Nihon University such as Masashi Kato, Kota Matsumoto and Seichiro Watanabe whose support for my experiment were very helpful.

In addition, I gratefully appreciate the financial support of JASSO (Japan Student services Organization) that made it possible to complete my thesis.

Finally, I would like to express my gratitude to my family for their moral support and warm encouragement.

## Research achievement

### [1]Published articles for scientific journal

- ① H. Itagaki, H. NUMAZAWA, K. Kishi, Y. Terashima, Y. Fujita, T. Awane, T. Asai, Ts. Takahashi, Y. Hirano, “Characteristic of a Repetitively Injected Spheromak in a Vertical Guid-Field”, *Plasma Fus.Res.*, The Japan Society of Plasma Science and Nuclear Fusion Research, **5**, pp S2031-1 – S2031-4 (2010).
- ② H. Itagaki, M. Inomoto, S. Kamio, Q.H. Cao, K. Takemura, K. Yamasaki, T.G. Watanabe, T. Yamada, “Development of a Quasi-steady Equilibrium Field System for Plasma Merging ST Startup Experiments on the UTST device”, *Plasma Fus. Res.*, The Japan Society of Plasma Science and Nuclear Fusion Research, **8**, pp 1402139-1 – 1402139-4 (2013).
- ③ H. Itagaki, T. Asai, M. Inomoto, Ts. Takahashi, “Mitigation of rotational instability of high beta FRC by double-side magnetized plasmoid injection”, *Phys. Plasma* (Submitted).
- ④ T. Asai, Ts. Takahashi, H. Matsunaga, H. Itagaki, Y. Matsuzawa, Y. Hirano, A. Hirose, “Active stability control of a high-beta self-organized compact torus”, In *23rd IAEA Fusion Energy Conference, Daejeon, Korea, ICC/P5-01*. (2010)
- ⑤ T. Asai, H. Itagaki, H. Numasawa, Y. Terashima, Y. Hirano, and A. Hirose, “A compact and continuously driven supersonic plasma and neutral source”, *Rev. Sci. Instrum.*, American institute of physics, **81**, 10E119 (2010).
- ⑥ T. Asai, H. Itagaki, Ts. Takahashi, M. Inomoto, L.C. Steinhauer, & To. Takahashi, “New control methods for stabilization and equilibrium of a field-reversed configuration” ICC(2011)
- ⑦ T. Asai, M. Yamazaki, H. TOMURO, H. ITAGAKI, M. Inomoto, To. Takahashi, “Generation of a Magnetized Plasma Shield by Means of a Rotating Magnetic Field for Innovative Space Transportation” *TRANSACTIONS OF THE JAPAN*

SOCIETY FOR AERONAUTICAL AND SPACE SCIENCES, AEROSPACE TECHNOLOGY JAPAN, **10**, Pc\_73-Pc\_78.

⑧S. Kamio, K. Yamasaki, K. Takemura, Q. Cao, T.G. Watanabe, H. Itagaki, T. Tsutsui, K. Ishigushi, R. Imazawa, T. Yamada, C.Z. Cheng, M. Inomoto, Y. Takase, Y. Ono, "Electron Acceleration by Magnetic Reconnection During Spherical Tokamak Merging Experiment", IEEJ Transactions on Fundamentals and Materials, The Institute of Electrical Engineers of Japan, **133**, 4, pp. 166-172 (2013)

[2]Presented paper for international conference

①H.Itagaki ,K.Kishi, H.Numazawa, Y.Terashima, T.Asai, T.Takahashi, H.Koguchi, 「Efficiency of flux build-up with high repetitive Spheromak injection」 『American Phys. Sci. meeting』 , Dallas, December,2008 (Poster)

②H. Itagaki, H. Numazawa, K. Kishi, Y. Terashima, Y. Fujita, T. Awane, T. Asai, Ts. Takahashi, Y. Hirano, 「Characteristic of a Repetitively Injected Spheromak in a Vertical Guid-Field」 『International Toki Conference 19』 Toki、 December, 2009 (Poster)

③H. Itagaki, T. Asai, K. Iguchi, Y. Kobayashi, Ts. Takahashi, M. Inomoto, To. Takahashi 「Active Plasma Shield Generated by RMF for a Space elevator」 『International Symposium on Space Technology and Science』, Tsukuba, July, 2009 (Oral)

④H. Itagaki, T. Asai, T. Takahashi, M. Inomoto, 「Active plasma shield」 『US-Japan CT-workshop』 , Kusatsu, September, 2009 (Oral)

⑤H. Itagaki, M. Goda, T. Asai, T. Takahashi, M. Inomoto, 「Coaxial helicity injection for Field-reversed configuration plasma generated by field-reversed theta-pinch technique」 『Open Systems 2012』 , Tsukuba, August, 2012 (Poster)

⑥H. Itagaki, M. Goda, T. Asai, T. Takahashi, M. Inomoto, 「Response of theta-pinch FRC to CHI」『US-Japan CT-workshop』, California, September, 2012  
(Oral)

⑦H. Itagaki, M. Kato, S. Watanabe, T. Asai, T. Takahashi, M. Inomoto, L.C. Steinhauer, 「Stability effect of a coaxial plasmoid injection on a Field-reversed configuration」『US-Japan CT-workshop』, Kobe, September, 2013 (Oral)

### [3]Japanese academic meeting and workshop

①板垣宏知、熊倉正巳、多米貴裕、岸香織、奥田真之介、島村信、林新也、浅井朋彦、高橋努「外部磁場領域におけるスフェロマックの高速繰り返し生成による磁束増幅効果」『日本物理学会 第63回年次大会』大阪、2008年3月  
(口頭発表)

②板垣宏知、岸香織、寺嶋悠紀、沼澤廣斗、浅井朋彦、高橋努、小口治久  
「Characteristic of spheromak with high repetitive injection in flux conserver region」『プラズマ・核融合学会第25回年会講演会』宇都宮、2008年12月 (ポスター発表)

③板垣宏知、井口一輝、小林由佳、浅井朋彦、井通暁「RMFによる荷電粒子線シールドの展開」『NIFS 共同研究 CT-RFP 研究会』多治見、2009年12月  
(口頭発表)

④板垣宏知、山崎翠、藤田侑希、高津幹夫、小口治久、井通暁、浅井朋彦  
「Formation and confinement properties of repetitively generated magnetized plasmoids by an IGBT inverter control」『PLASMA2011』、金沢、2011年11月 (ポスター発表)

⑤板垣宏知、浅井朋彦、井通暁、高橋俊樹「FRC への同軸ヘリシティ入射効果」  
『NIFS 共同研究 CT-RFP 研究会』多治見、2012年12月 (口頭発表)

⑥板垣宏知、浅井朋彦、井通暁、高橋努、L.C. Steinhauer、高橋俊樹「磁場反

転配位における磁化プラズモイド入射の不安定性抑制効果」『プラズマ・核融合学会第30回年会講演会』 東京、2013年12月

- ⑦板垣宏知、浅井朋彦、井通暁、高橋努、L. C. Steinhauer, 高橋俊樹「FRC への磁化プラズモイド入射による回転不安定性の抑制」『NIFS 共同研究 CT-RFP 研究会』 多治見, 2013年 12月 (口頭発表)